1996ApJ...457..460W

THE ASTROPHYSICAL JOURNAL, 457:460–489, 1996 February 1

HOMOGENEOUS VELOCITY-DISTANCE DATA FOR PECULIAR VELOCITY ANALYSIS. II. CALIBRATION OF FIELD SAMPLES

JEFFREY A. WILLICK,[1] STÉPHANE COURTEAU,[2] S. M. FABER,[3] DAVID BURSTEIN,[4]
AVISHAI DEKEL,[5] AND TSAFRIR KOLATT[5,6]

Received 1995 June 1; accepted 1995 August 4

ABSTRACT

This is the second in a series of papers in which we assemble and analyze a homogeneous catalog of peculiar velocity data. In Paper I, we treated two Tully-Fisher (TF) cluster samples. Here, we study four TF field samples: the *I*-band sample of Mathewson, Ford, & Buchhorn, the *r*-band samples of Willick and Courteau-Faber, and the *H*-band sample of Aaronson et al. as revised by Tormen & Burstein. In Paper III, we will combine these spiral samples with elliptical data to form the Mark III Catalog of Galaxy Peculiar Velocities, which will be used as input for POTENT and other velocity analyses.

We derive the TF slope and scatter separately for each sample, correcting for selection biases and self-consistency determining internal-extinction coefficients. We find no evidence for a luminosity dependence of internal extinction. We fit both forward and inverse TF relations and, by comparing the two, validate the bias corrections applied to the forward fits. By matching TF distances for several hundred galaxies common to two or more samples, we determine the relative zero points of the various TF relations. The global zero point is set by the Han-Mould TF calibration carried out in Paper I.

We calibrate the TF relations after grouping field galaxies in redshift space, making conservative use of preliminary TF relations based on Hubble flow distances. The differences between the preliminary and final TF scatter estimates indicate typical radial peculiar velocities of $\sim$250–300 km s^{-1}. We find observed scatters $\sigma_{\rm TF} \approx 0.38$–0.43 mag for the *r*- and *I*-band samples, larger than many recent estimates, and estimate the intrinsic TF scatter to be $\sim$0.30 mag. Based on simulated catalogs, we find that our observed scatter estimates are good to $\lesssim 5\%$.

Subject headings: galaxies: distances and redshifts — large-scale structure of universe

1. INTRODUCTION

The measurement and analysis of galaxy peculiar velocities are emerging as important tools for cosmology. In the gravitational instability scenario for structure formation, the amplitude and coherence scale of the peculiar velocity field uniquely reflect those of the underlying mass-density field, independent of possible biasing of dark versus luminous matter. Density fluctuations inferred from peculiar velocities may be compared with those inferred from cosmic microwave background fluctuations (Górski et al. 1994), providing a powerful consistency check on the gravitational instability picture (Babul et al. 1994). To the extent the relationship between galaxies and mass can be accurately modeled, comparison of peculiar velocity and redshift survey data yields a value of the density parameter Ω_0 (see, e.g., Dekel 1994; Strauss & Willick 1995).

Peculiar velocity analyses require large samples of galaxies with redshift-independent distance measurements. Two methods for obtaining such measurements are especially useful for such studies: the Tully-Fisher (TF) relation for spirals and the D_n-σ relation for ellipticals. Several groups have independently obtained a substantial quantity of TF and D_n-σ data over the last decade. These samples must be carefully processed and combined in order to produce a homogeneous data set with wide sky coverage, as is needed to address the scientific issues mentioned above.

This is the second in a series of papers in which our goal is first to compile a large, homogeneous catalog of TF data, combining it in the process with previously published D_n-σ data, and subsequently to use this catalog for rigorous peculiar velocity analysis. In Paper I (Willick et al. 1995a), we presented our basic methods, notation, and philosophy and carried out TF calibrations for the cluster samples of Han, Mould, and coworkers (HM) and Willick (W91CL). Familiarity with Paper I is essential for the reader of this and later papers in the series. In this paper, we continue our analysis of the six separate samples that comprise our TF database, treating now the field-galaxy samples of Mathewson, Ford, & Buchhorn (1992; MAT), Willick (1991; W91PP), Courteau-Faber (Courteau 1992; CF), and Aaronson et al. (1982, recently revised by Tormen & Burstein 1995; A82). In Paper III (Willick et al. 1995b) we will present the final calibrated TF and D_n-σ data in tabular form as the Mark III Catalog of Galaxy Peculiar Velocities, and perform a variety of statistical tests pertaining to the validity of the catalog for velocity analysis. In Papers IV (Faber et al. 1996) and V (Dekel et al. 1996), we will carry our velocity analyses of the catalog using graphical methods and the POTENT velocity and density reconstruction algorithm (Dekel, Bertschinger, & Faber 1990; Dekel et al. 1993). Preliminary analyses of the Mark III catalog have been carried out by Courteau et al. (1993), Faber et al. (1993, 1994), Dekel

---

[1] Carnegie Observatories, 813 Santa Barbara Street, Pasadena, CA 91101-1292. Current address: Department of Physics, Stanford University, Stanford, CA 94305-4060

[2] NOAO/KPNO, 950 N. Cherry Avenue, Tucson, AZ 85726-6732.

[3] UCO/Lick Observatory, University of California, Santa Cruz, Santa Cruz, CA 95064.

[4] Department of Physics and Astronomy, Arizona State University, Box 871504, Tempe, AZ 85287-1504.

[5] Racah Institute of Physics, The Hebrew University of Jerusalem, Jerusalem 91904, Israel.

[6] Harvard-Smithsonian Center for Astrophysics, 60 Garden Street, Cambridge, MA 02138.

(1994), Kolatt (1995), Hudson et al. (1995), and Strauss & Willick (1995).

This paper goes beyond Paper I in one important respect. Because we are treating field samples here, it is not obvious how, if at all, to group the galaxies when calibrating the sample TF relations. An alternative to grouping galaxies would be to adopt models of the peculiar velocity field such that galaxy distances could be assigned from their redshifts and sky positions. However, for reasons discusssed in Paper I, § 2, we have chosen to eschew this approach. We have thus developed a *redshift-space grouping algorithm*, which enables us to place field galaxies into groups and, subsequently, to fit TF relations in the same way we did for the cluster samples in Paper I. Because the algorithm also uses TF-distance information—albeit in an extremely conservative way (§ 2.2.2)—we determine preliminary TF relations from Hubble flow fits. We will argue that our group analysis enables us to constrain the values of the TF scatters for the various samples to good ($\lesssim 5\%$) accuracy. This is essential because the TF scatter dominates the random and systematic errors in peculiar velocity studies. We will use the groups not only for calibrating TF relations but also later in the POTENT velocity-field reconstruction (Hudson et al. 1995; Paper V). When we treat groups, rather than individual galaxies, as tracers of the velocity field, Malmquist bias effects—which are inversely proportional to the number of objects in a group—can be made quite small (Kolatt 1995). In Paper III we will present the group-membership data in tabular form.

Another issue we investigate here, but did not in Paper I, is the possibility that internal-extinction corrections are luminosity dependent. Giovanelli (1995) has recently claimed that the I-band internal-extinction coefficient ($C_{\rm int}^I$ in our terminology) varies from ~ 0.5 for the faintest galaxies to ~ 1.3 for the brightest galaxies. Such an effect, if it exists and were neglected, would systematically influence velocity-field analyses. More distant (typically more luminous) galaxies would be undercorrected and more nearby (typically fainter) galaxies would be overcorrected for internal extinction, which would generate false signals of flow convergence at the mean depth of the sample. We carry out a detailed test for this effect using the MAT and W91PP samples.

The final task of this paper is to complete the process of homogenization by ensuring that the various TF samples produce a uniform set of distances. We do this by adjusting the individual sample TF zero points to minimize distance-modulus differences for galaxies common to two or more samples. The global zero point for the Mark III catalog is determined by that of the HM sample, which was derived in Paper I. At the end of the paper, we present fully calibrated forward and inverse TF relations for each spiral sample. The outline of this paper is as follows: In § 2, we carry out the TF calibration of the MAT sample; in the process, we also describe and motivate our use of the grouping algorithm. The TF calibrations of the W91PP, CF, and A82 samples are presented in §§ 3, 4, and 5, respectively. In § 6, we place the samples on a common zero point. In § 7, we further discuss our TF scatter estimates and estimate the intrinsic scatter of the TF relation. We summarize our main results in § 8.

2. THE MAT SAMPLE

The full MAT TF sample consists of the 1355 galaxies for which Mathewson et al. (1992, hereafter MAT92) presented data. As discussed in Paper I, we adopt the raw data from MAT92 but apply our own corrections to them. Thus, we have recomputed inclinations, velocity widths, and apparent magnitudes using procedures we will detail in Paper III. We have reduced the size of the full MAT sample, using exclusion criteria also to be detailed in Paper III. The most important of these criteria are the imposition of a photographic-diameter limit of 1'.6, to be discussed further below, a minimum inclination of 35°, and a minimum η-value[7] of -0.42. The last criterion excludes extremely faint galaxies, which may deviate from the TF relation of their more luminous counterparts. The reduced sample consists of 1220 galaxies, which we use here for TF calibration and later in the series for the POTENT analysis. Peculiar velocity analyses are not necessarily restricted to this 1220 galaxy subsample, however, and in Paper III we will present data for the full MAT sample.

2.1. *Selection Criteria Relations for MAT*

The first step toward TF calibration is quantitative characterization of sample-selection criteria (see Paper I). This is needed to implement the bias-correction procedure of Willick (1994, hereafter W94). The most important selection criterion for MAT in terms of bias effects is the diameter limit. To account for its effect on TF calibration, we need to derive a relation between the photographic diameters and the TF observables. Such a relation gives the sample-selection probability as a function of apparent magnitude and line width; this selection probability in turn yields the apparent magnitude bias in the TF calibration procedure (see W94, § 4.1). The other selection criterion that relates to selection bias is the η-limit, which affects only the inverse TF calibration (§ 2.2.6). As this limit is imposed directly on a quantity that is entering the TF analysis (as opposed to the "indirect" effect of the diameter limit), it requires no further analysis here.

Two issues complicate the MAT diameter limit. The first is that the sample is drawn from three different catalogs. The great majority of sample objects is taken from the ESO-Uppsala catalog of galaxies (Lauberts 1982; ESO), but a small percentage is drawn from the MCG (Vorontsov-Veliaminov & Arhipova 1968) and UGC (Nilson 1973) catalogs. The photographic diameters for the ESO and non-ESO objects are not given on the same system (Lahav, Rowan-Robinson, & Lynden-Bell 1988), and it is not clear that the same diameter limit would apply to the two subsets even if the diameter systems were mutually consistent. However, in view of the very small number of non-ESO objects (five UGC and 42 MCG galaxies in the 1220 galaxy calibration subsample, or $\sim 4\%$), the effect of this diameter ambiguity will be quite small, and we choose to ignore it in the TF calibration.

The second issue is the actual value of the diameter limit. According to MAT92, the sample was selected to an ESO photographic-diameter limit of 1'.7. However, this statement is not borne out by the sample data themselves. The left panel of Figure 1 shows a histogram of ESO photographic diameters ($D_{\rm ESO}$) for the full MAT sample. There are nearly as many objects with $D_{\rm ESO} = 1'.6$ as with $D_{\rm ESO} = 1'.7$; the number of sample objects drops precipitously for diameters smaller than 1'.6. The right panel of Figure 1 plots $D_{\rm ESO}$ as a function of redshift. There does not appear to be a significant decrease in the effective minimum diameter with increasing redshift. In the TF analysis, therefore, we will take the limiting diameter to be

---

[7] In Paper I, § 2.1, we defined η as $\log \Delta v - 2.5$, where Δv is the twice the rotation velocity of the galaxy.

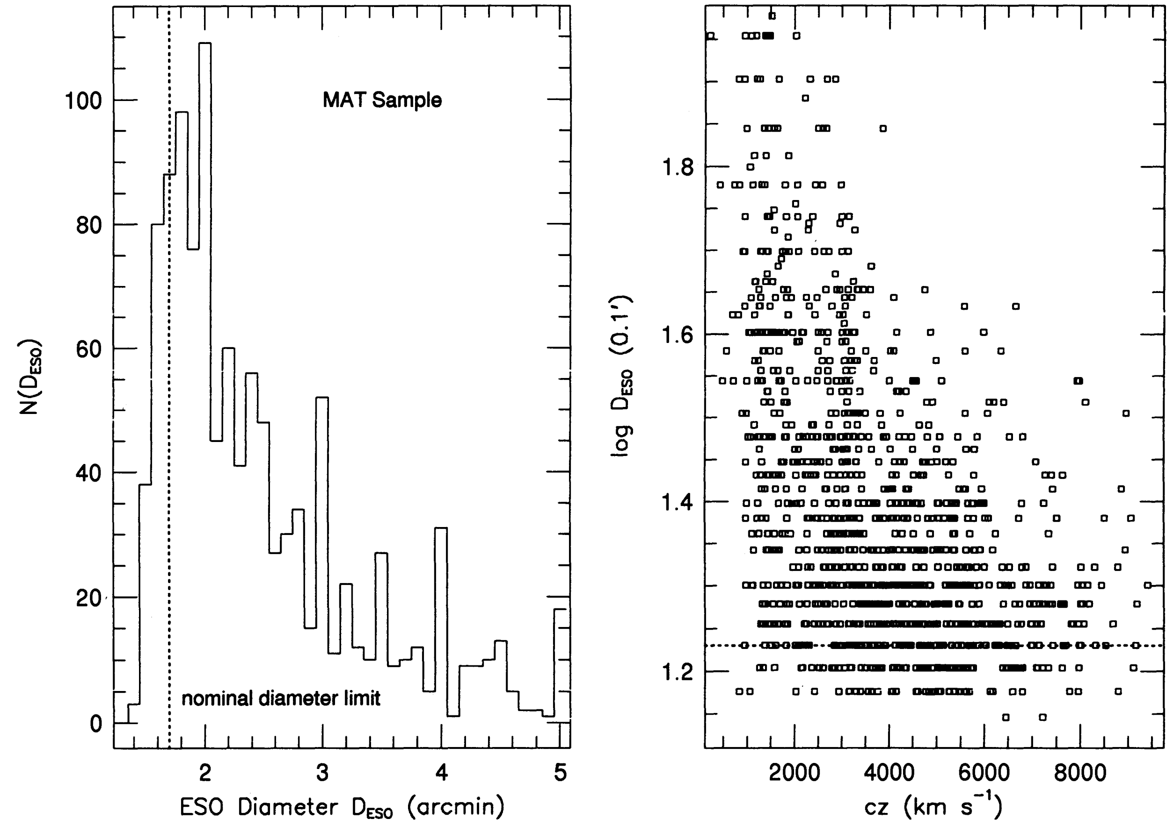

FIG. 1.—*Left*, histogram of apparent diameters, in 0.′1 bins, for ESO galaxies in the MAT sample; *right*, log $D_{\rm ESO}$ (in units of 0.′1) plotted against cosmic microwave background–frame redshift for ESO galaxies in the MAT sample. In each panel, the dotted line shows the nominal ESO diameter limit of 1.′7 for the sample as reported by Mathewson et al. (1992). It is apparent that the actual diameter limit is somewhat smaller.

1.′6, excluding all smaller galaxies and adopting this limit in the W94 bias-correction procedure. We further validate this choice of diameter limit in § 2.2.7. However, in the analysis of the relationship between the ESO diameters and the TF observables, we will be more conservative and limit the analysis to objects with $D_{\rm ESO} \geq 1.'7$. This ensures that the $D_{\rm ESO}$-m_I relation we now derive—on which the TF calibration bias-correction procedure critically depends—is unaffected by the diameter-limit ambiguity.

We assume that the logarithm of the ESO diameter expressed in units of 0.′1, log $D_{\rm ESO}$, is linearly related to the observables that enter into the TF relation (the I-band apparent magnitude m_I, the velocity-width parameter η, the logarithm of axial ratio $\mathscr{R}$, and the Galactic extinction A_B) as well as log redshift. When we fit such a relation to the ESO galaxies that satisfy $D_{\rm ESO} \geq 1.'7$, we obtain the coefficients shown in Table 1. We remind the reader (see Paper I, § 3.1) that such a fit is itself strongly biased because the fitted variable (log diameter) is subject to a strict limit; hence we apply the iterative bias-correction procedure of W94 in carrying out this fit. In addition, we have excluded from the fit objects with $m_I >$ 14.1 mag in order to minimize the number of highly biased objects that can undermine the validity of the bias-correction procedure. The coefficients of η and A_B listed in Table 1 are identically zero because the fitted values of these parameters were insignificant. This is consistent with the result obtained for HM South (see Paper I, § 3.1.2), in which a very similar relation for log $D_{\rm ESO}$ was obtained (see Paper I, Table 2). In the left panel of Figure 2, we plot the bias-corrected values of log $D_{\rm ESO}$ versus raw I-band magnitude. The diameter limit for the fit is shown as a dotted line. As in Paper I, we see that the bias-corrected diameters can be smaller than the limit. This is the ultimate source of the selection biases that will affect the MAT TF calibration.

When η rather than log cz is included in the fit, a significant value of the η-coefficient results. However, the scatter is then larger than that shown in Table 1. Inclusion of both log cz and η in the fit does not lead to improvement. We thus assume that

TABLE 1

FIT COEFFICIENTS FOR MAT

QUANTITY PREDICTED	CONSTANT	COEFFICIENT OF m_I	η	A_B	$\mathscr{R}$	log cz − 3.7	σ
log $D_{\rm ESO}$......	3.128	0.160	0.000	0.000	0.323	0.320	0.120

NOTE.—Coefficients of the indicated quantities in the linear relation for log $D_{\rm ESO}$ for the MAT sample, along with the rms dispersion for this relation.

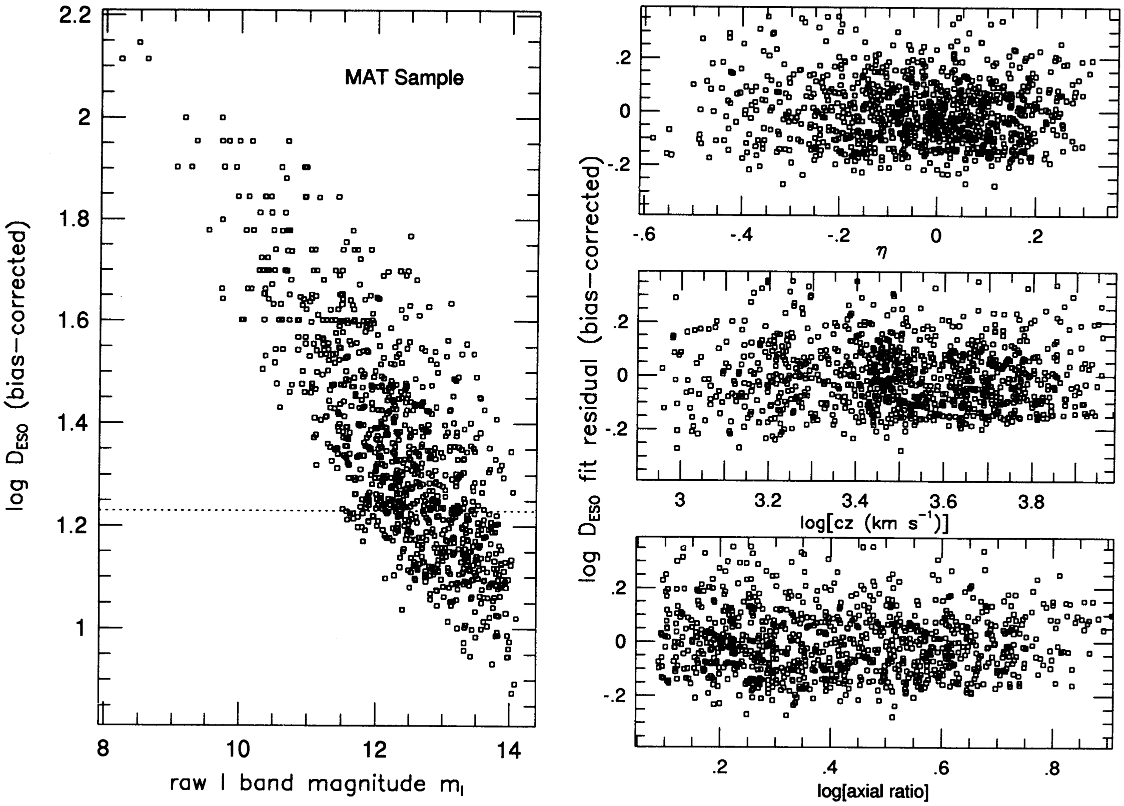

FIG. 2.—Results of fitting log D_{ESO} to the TF observables for the MAT sample. The left panel shows bias-corrected values of log D_{ESO} plotted against the raw I-band magnitudes. The right panel shows residuals from this fit plotted against η (*top*), log redshift (*middle*), and log axial ratio (*bottom*). The apparent truncation of the residuals at about -0.2 dex results from the strongly biased nature of the fit; see § 2.1 for details.

the relation for log D_{ESO} is η-independent; the redshift term then presumably indicates a distance dependence. However, one must recognize that the redshift and velocity-width dependences are difficult to disentangle. For the forward TF fits, this issue is relative unimportant,[8] but for the inverse TF fits the η-dependence is crucial. In the right panels of Figure 2, we plot residuals from the best fit with respect to η, log cz, and axial ratio. No remaining trends are seen, indicating the adequacy of our fits. However, it is apparent that the fit residuals do not possess a Gaussian distribution. The reason for this is not inherent non-Gaussianity but rather the strongly biased nature of the fit. Although the bias-correction procedure gives us a valid mean relation, it cannot restore the uniform distribution of residuals about expected values.

2.2. *Calibration of the MAT TF Relation*

Unlike HM and W91CL, the MAT sample does not neatly divide into well-defined galaxy clusters. MAT92 provide a list of nominal clusters, but these are for the most part poorly defined; many have large redshift-space spreads, while there is scant evidence in redshift maps of finger-of-god effects at their locations. They are thus unlikely to be clusters in the true sense. Moreover, our realistic estimate of the MAT TF scatter ($\sim$0.43 mag; see below) greatly exceeds the 0.32 mag estimated by MAT92 from fits to the nominal clusters, suggesting that the nominal clusters are unrepresentative of the sample as a whole. We will instead use the entire 1220 galaxy subsample for TF calibration. This raises a number of complicated issues, as we now discuss.

For calibration, we need a way to assign "TF-orthogonal" distances to sample galaxies (see Paper I, § 2). As we have foresworn the approach of using detailed peculiar velocity models, we must instead assign field galaxies to groups whose individual members lie at a common distance. But the construction of such groups presents a dilemma. The most obvious criterion for group membership is redshift-space proximity. But it is possible that two objects, along a given line of sight and with very similar redshifts, are in reality widely separated. This would occur if their relative peculiar velocity of approach were comparable to their Hubble velocity of separation. To remedy this situation, we need to invoke the TF information. Yet, at the outset, we do not even have a TF relation to use for this purpose.

In what follows, we resolve this dilemma through a combination of the two basic approaches to modeling distances. First, we obtain a preliminary TF relation by adopting a "peculiar velocity" model, but that model is the null hypothesis: that peculiar velocities are everywhere negligible. We thus build into our preliminary TF calibration only the assumption of which we are most certain, that the universe is expanding according to Hubble's law. If there are true peculiar velocities, they will manifest themselves as increased apparent TF scatter, but the TF zero point and slope thus obtained will be sufficiently accurate to move on. In the second step, we group objects in redshift space, but modify these groups in a well-

---

[8] The forward fits are, however, affected to some degree: the coefficient of m_I in the relation for log D_{ESO}, and consequently the "β-parameter" in the W94 bias-correction procedure, is larger when the relation is modeled in terms of η rather than log cz.

defined way using the preliminary TF relation. A new TF relation may then be fitted to the groups. The free parameters in such a fit are a single TF slope and relative distance moduli for each group. The discussion surrounding equation (18) of Paper I gives the details of how such a fit is carried out. The TF slope and scatter that result from the group fit are correct to within statistical errors, provided the groups are realistic. Much of the discussion to follow will be concerned with ensuring that they are.

2.2.1. *Preliminary Hubble Flow Fits*

Forward TF Hubble flow fits proceed as follows. First, we define a "Hubble absolute magnitude" $M_{\rm H}$ for a galaxy with observed apparent magnitude m and redshift cz (measured in km s^{-1}):

$$M_{\rm H}(m, cz) = m - 5 \log cz \, . \tag{1}$$

We then minimize the quantity

$$\sum_i \frac{[M_{\rm H}(m_i, cz_i) - (A - b\eta_i)]^2}{\sigma_0^2 + f^2(\sigma_v/cz_i)^2} \tag{2}$$

with respect to the TF parameters A and b. Here σ_0 is an estimate of the true TF scatter, σ_v an estimate of the radial velocity dispersion about pure Hubble flow, and $f = 5/\ln 10 \approx 2.171$. The fit is insensitive to the precise values of σ_0 and σ_v, and we adopt $\sigma_0 = 0.40$ mag and $\sigma_v = 300$ km s^{-1}. A single fit yields biased values of the parameters because of the diameter limit. The bias-correction procedure of W94 is therefore applied, and the fit is iterated until convergence (see Paper I, § 3.2, for details).

The redshift cz that appears in equation (2) is a frame-dependent quantity. We carry out the fits in three reference frames—the cosmic microwave background (CMB), Local Group (LG), and heliocentric frames—and will simply adopt the TF relation from the smallest scatter fit. The fits involved 1219 of the 1220 MAT galaxies; one very nearby ($cz = 226$ km s^{-1}) object was excluded. The resulting TF parameters are given in Table 2. Note that the scatter σ is smallest when heliocentric redshifts are used. Since the CMB presumably defines the true cosmic "rest frame," the smaller scatter of the heliocentric fit most likely reflects large-scale departure from Hubble flow in which the MAT sample participates. The excellent agreement between the TF zero points and slopes for the heliocentric and CMB frames is reassuring, however. The heliocentric Hubble flow fit provides us with a preliminary TF relation and a rough estimate of its scatter, $\sigma \approx 0.47$ mag. To the degree the Hubble flow model is imperfect, this value is larger than the true MAT TF scatter. However, we have no reason to suppose the TF parameters A and b derived from the above exercise are seriously in error. Thus, we are now equipped to apply the grouping algorithm.

TABLE 2

MAT TF RELATION FROM HUBBLE FLOW FITS

Reference Frame	A	b	σ (mag)	N_σ
Heliocentric	−5.828	6.808	0.467	1209
CMB	−5.828	6.827	0.502	1207
Local Group	−5.720	6.961	0.484	1208

NOTES.—Parameters that result from fitting a forward TF relation to the MAT sample, under the assumption of uniform Hubble flow in a heliocentric, CMB, and LG frame of reference. N_σ is the number of objects (those with fit residuals less than 1.75 mag) used in the scatter computation. In each case a total of 1219 objects participated in the fit.

2.2.2. *The Grouping Algorithm: Motivation and Description*

Before we describe the grouping algorithm, a word about its limitations is in order. It is *not* our intention to identify groups of galaxies whose dynamical characteristics are in any sense well defined. We do not, in particular, seek to identify groups that are gravitationally bound. Rather, we aim to form groups whose only defining characteristic is that members lie at a common distance. Here, "lying at a common distance" should be understood as "possessing a true depth undetectable by the TF relation." The distances to objects in a group may differ, provided this difference is small relative to the TF error. Groups with these specific properties are adequate for the purpose of calibrating the TF relation and efficiently reducing Malmquist bias.

The algorithm uses two fundamental criteria for assigning galaxies to groups. The first is *redshift-space proximity*; the second is "TF-distance" proximity. The first criterion is enforced strongly in the sense that galaxies must be within ~150 km s^{-1} in radial velocity, and about twice that in transverse velocity, of a common center for inclusion in a group (the actual group sizes depend on redshift, as described below). The groups are thus very "tight" in redshift space. This reflects the basic physical assumption that underlies the algorithm, namely that small-scale, random motions ("noise") relative to the mean velocity field of galaxies are small ($\lesssim 200$ km s^{-1}). By contrast, the TF-distance criterion is applied extremely conservatively—ultimately at a $\gtrsim 3\ \sigma$ level. The TF-distances of two group members may thus differ greatly (typically by ~1000–2000 km s^{-1}), while their redshifts may differ by a few hundred km s^{-1} at most.

The algorithm requires three basic input parameters: a *radial velocity spread parameter* σ_r, a *transverse velocity spread parameter* σ_t, and the TF *input scatter* $\sigma_{\rm in}$. Galaxies are provisionally grouped if their radial velocities differ by less than σ_r and their transverse velocity difference (roughly, redshift times angular separation) is less than σ_t. In practice, we have σ_r and σ_t increase with radial velocity in order to form groups efficiently at larger distances, where the sampling becomes more dilute. While this means that the redshift-space (and presumably real space) group sizes increase with redshift, this is acceptable since the TF-distance uncertainty does so as well. In the left panel of Figure 3, we plot the adopted forms of σ_r and σ_t for the MAT-sample grouping as a function of redshift. The groupings of the other samples (W91PP and A82) use similar forms of σ_r and σ_t. The right panels show the rms transverse (*top*) and radial (*bottom*) redshift-space sizes of the MAT groups actually formed versus σ_t and σ_r. Note in particular that for $\sigma_r \lesssim 400$ km s^{-1} (i.e., $cz \lesssim 5000$ km s^{-1}) typical rms group sizes are $\lesssim 150$ km s^{-1} in radial velocity.

The input scatter $\sigma_{\rm in}$ ought ideally to be roughly equal to the true TF scatter σ. In practice, we do not know σ at the outset, so we will treat $\sigma_{\rm in}$ as a variable input parameter; as described below, we will use the variation of the output-group properties as a function of $\sigma_{\rm in}$ to choose its optimal value. The algorithm converts $\sigma_{\rm in}$ into an equivalent fractional distance error $\Delta_{\rm in} = (\ln 10/5)\sigma_{\rm in} \approx 0.46\sigma_{\rm in}$. Each galaxy is assigned a TF-inferred distance

$$d = 10^{0.2[m-(A-b\eta)]} \, , \tag{3}$$

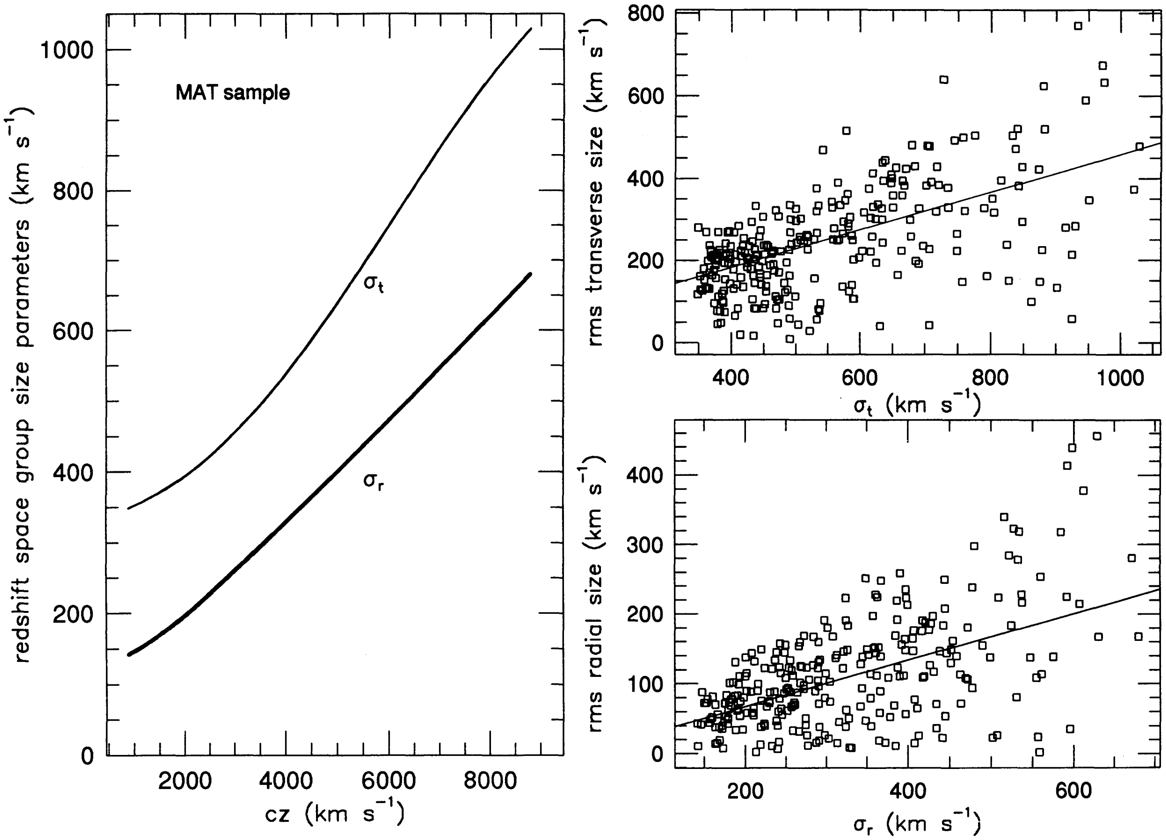

FIG. 3.—*Left:* Grouping-algorithm input parameters σ_r and σ_t, which control redshift-space radial and transverse group sizes, respectively, plotted against redshift. The plots depict the redshift dependence of these parameters used for the MAT-sample grouping; very similar dependences were used for the W91PP and A82 sample groupings as well. *Right:* The top panel shows the rms transverse sizes plotted against σ_t, and the bottom panel rms radial sizes plotted against σ_r, of the MAT-sample groups generated by the algorithm. The lines drawn through the points are the approximate fits: mean rms transverse group size $\approx 0.46\sigma_t$; mean rms radial group size $\approx 0.33\sigma_r$.

using the parameters of the preliminary TF relation, and an apparent radial peculiar velocity $u = cz - d$. We do not concern ourselves at this point with biases in d or u, nor with the possible inaccuracy of the input TF parameters. Because we are using the TF information very conservatively, our results are insensitive to such second-order effects. Galaxies that have passed the redshift-space proximity test are now grouped if their apparent peculiar velocities differ by less than $\sim 3\Delta_{\rm in} d$ (the actual condition is somewhat more complicated and accounts for the fact that the Gaussian distribution of TF residuals converts to a lognormal distribution of distance errors). This last grouping criterion is equivalent to requiring that grouped objects have TF magnitude residuals $\lesssim 3\sigma_{\rm in}$.

The algorithm proceeds in several stages. In the first, all pairs of galaxies are tested for association. The grouped pairs are then merged with other pairs with which they share a member, thus forming larger groups. An effort is then made to amalgamate these groups by testing whether any two are close enough in redshift and TF-distance space; the latter test takes into account the reduced distance uncertainty with increasing number of members. A final effort is made to place ungrouped objects, which were not paired initially, into the updated set of groups. Once this is done, the groups are "exploded," i.e., their members are returned to the pool of individual objects; the group redshift-space positions and TF-distances remain as the "seeds" for subsequent passes of the algorithm. In these subsequent passes, which are iterated until the makeup of the groups is unchanging, individual objects undergo the redshift-space and TF-distance–space proximity tests not with each other but with the current group centers. At the end of each iteration, group centers are recomputed. Upon convergence, the algorithm returns the group positions in redshift and TF-distance space and a list of their individual members.

The greatest danger in the grouping approach to TF calibration is that we will use the preliminary TF relation too liberally in forming groups. Consider a group of redshift-space neighbors. Suppose first that they constitute a real-space group as well. Too liberal a use of the TF information occurs when the input scatter $\sigma_{\rm in}$ is too small. This would lead us to exclude some actual group members on the grounds that their TF residuals appear too large. The remaining objects would still be a group, but they would exhibit a TF relation with artificially diminished scatter. Another danger of the grouping approach is too conservative a use of the TF information, which occurs when $\sigma_{\rm in}$ is too large. Suppose that our group of redshift-space neighbors actually consists of a real-space group plus an admixture of superpositions. If $\sigma_{\rm in}$ is too large, we will fail to exclude the superpositions. The redshift-space group will then exhibit an inflated TF scatter because its members are not actually equidistant.

2.2.3. *The Grouping Algorithm: Application*

Let us refer to the scatter of the TF relation fitted to the groups as the "output scatter," or $\sigma_{\rm out}$. The discussion above

1996ApJ...457..460W

suggests that $\sigma_{\rm out}$ will vary with $\sigma_{\rm in}$ in a characteristic way. When $\sigma_{\rm in}$ is far below the true TF scatter σ, $\sigma_{\rm out}$ will underestimate σ but will exceed $\sigma_{\rm in}$. This occurs because, although we exclude from group membership galaxies whose TF residuals are greater than $\sim 3\sigma_{\rm in}$, the remaining objects will retain some signature of the true scatter. On the other hand, when $\sigma_{\rm in}$ is much greater than σ, the output scatter will fall below $\sigma_{\rm in}$. This occurs because taking $\sigma_{\rm in}$ to be infinitely large corresponds to a pure redshift-space grouping. Such a grouping can be no worse than modeling distances by pure Hubble flow, and a Hubble flow TF fit (§ 2.2.1) has finite scatter. It follows that a plot of $\sigma_{\rm out}$ versus $\sigma_{\rm in}$ lies initially above the unity line, then crosses this line, and finally asymptotes to a limiting value. If we can calibrate the $\sigma_{\rm out}$-$\sigma_{\rm in}$ diagram, we can hope to deduce from it the correct value of the TF scatter.

The grouping algorithm is sufficiently complex that the precise location on the $\sigma_{\rm out}$-$\sigma_{\rm in}$ graph of "truth" cannot be predicted a priori. Thus, we will calibrate the $\sigma_{\rm out}$-$\sigma_{\rm in}$ diagram using simulated TF data sets that have been generated by Kolatt and coworkers (Kolatt 1995; Kolatt et al. 1996). The reader is referred to those references for details; here we note only that the redshift and apparent magnitude distributions of the simulated TF samples resemble those of the true samples and that the simulated samples are subject to selection biases that mimic those of the real data. The dynamics of the N-body simulation from which the mock TF samples were generated are those of an $\Omega = 1$ universe. The simulated MAT sample has a true TF slope $b = 6.71$ and a true TF scatter $\sigma = 0.42$ mag. Hubble flow TF relations were fitted to the simulated MAT sample, just as was done with the real data. The TF parameters corresponding to the smallest scatter (0.48 mag) where then used in the grouping algorithm.

Figure 4 shows the results of applying the grouping algorithm to the simulated MAT sample. The four panels show the output scatter $\sigma_{\rm out}$, the TF slope fitted to the groups, the mean number of objects per group $\langle n_g \rangle$, and the percentage of total objects grouped plotted against the input scatter $\sigma_{\rm in}$. The slope and scatter error bars were computed under the assumption that the output scatter was correct. The $\sigma_{\rm out}$-$\sigma_{\rm in}$ diagram exhibits the behavior predicted above. The output scatter significantly underestimates the true scatter as long as $\sigma_{\rm out}$ is at least $\sim 10\%$ larger than $\sigma_{\rm in}$. For $\sigma_{\rm in}$ in the range $\sim(0.95$–$1.25)\sigma_{\rm out}$, the output scatter is equal, to within the errors, to the true scatter. When $\sigma_{\rm in}$ exceeds $\sigma_{\rm out}$ by $\sim 30\%$ or more—in the present case, for $\sigma_{\rm in} \gtrsim 0.60$ mag—$\sigma_{\rm out}$ significantly overestimates the true scatter. However, $\sigma_{\rm out}$ asymptotes to ~ 0.45 mag as $\sigma_{\rm in}$ is made very large. This limiting value is significantly smaller than the Hubble flow scatter for the simulated sample. Thus, even a pure redshift-space grouping provides a better distance model than Hubble flow, in which redshift corresponds precisely to distance regardless of angular position.

In the top right panel of Figure 4, we see that the TF slope fitted to the groups exhibits a marginally significant trend over the full range of $\sigma_{\rm in}$. However, for the restricted range of "valid" $\sigma_{\rm in}$ ($\sim$0.40–0.55 mag) the output slopes are in good agreement with one another, as well as with the true TF slope, and show no trend. This suggests that the group TF calibration will not incur a systematic slope error provided that an

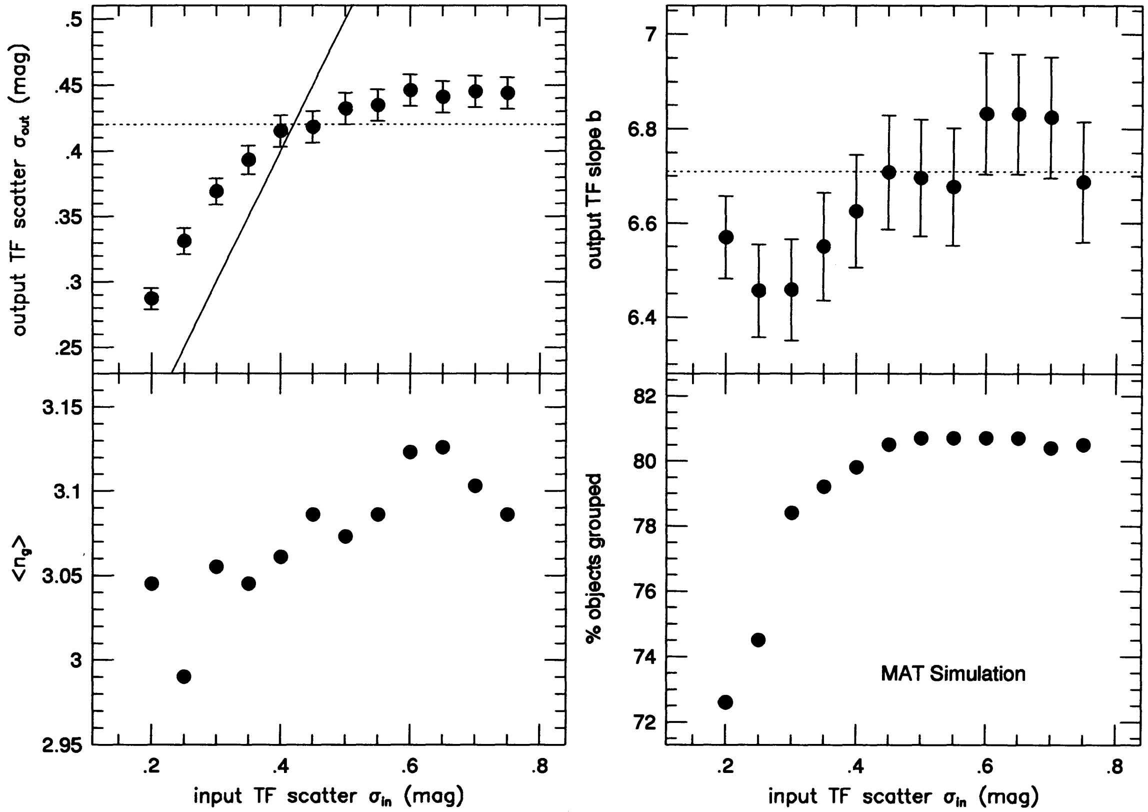

FIG. 4.—Four output parameters of the grouping algorithm applied to the simulated MAT sample, plotted as a function of the input scatter $\sigma_{\rm in}$: the scatter of the TF relation fitted to the groups, $\sigma_{\rm out}$ (*upper left*), the slope of the TF relation fitted to the groups (*upper right*), the mean number of objects per group (*lower left*), and the percentage of total sample objects grouped (*lower right*). In the upper left panel, the solid line is the unity line $y = x$. The dotted lines indicate the true TF scatter (*upper left*) and slope (*upper right*) of the simulated MAT sample. The scatter and slope error bars are 1 σ statistical estimates.

appropriate value of $\sigma_{\rm in}$ is used. The lower right panel provides a further diagnostic of the "correct" value of $\sigma_{\rm in}$. The percentage of objects grouped rises sharply and then plateaus as $\sigma_{\rm in}$ increases; the proper value of $\sigma_{\rm in}$ occurs near the onset of the plateau region. The behavior of $\langle n_g \rangle$ is more erratic; our application of the algorithm to other samples will confirm that $\langle n_g \rangle$ is not a reliable diagnostic, and we will not use it to constrain $\sigma_{\rm in}$.

Figure 5 shows the same information for the grouping algorithm applied to the real MAT sample. Figure 5 bears an overall qualitative resemblance to Figure 4, suggesting that we may indeed use the simulation as a guide for interpreting the real data. From the simulation we deduced that $\sigma_{\rm out}$ is a good estimate of the true scatter when $\sigma_{\rm in}/\sigma_{\rm out} \approx 0.95$–$1.25$. Applying this rule of thumb to the upper left panel of Figure 5 indicates that $\sigma_{\rm out}$ provides a good estimate of the true MAT TF scatter for 0.40 mag $\leq \sigma_{\rm in} \leq$ 0.55 mag, corresponding to $\sigma_{\rm out} =$ 0.415–0.445 mag. The upper right panel of Figure 5 shows that while there is a slight overall trend in the fitted slopes, for the valid range of $\sigma_{\rm in}$ the slopes are consistent within the errors and manifest no trend. The lower right panel shows that for $\sigma_{\rm in} \gtrsim 0.40$ mag the percentage of total objects grouped is at the onset of or within the plateau regime, consistent the range of valid $\sigma_{\rm in}$ estimated from the $\sigma_{\rm out}$-$\sigma_{\rm in}$ diagram. The output scatter asymptotes to ~0.45 mag, somewhat greater than our estimate of the true scatter. This behavior, too, is consistent with what was seen for the simulation.

While Figures 4 and 5 bear an overall resemblance to one another, the correspondence is not exact. The "turnovers" in the $\sigma_{\rm out}$ and percentage of objects grouped versus $\sigma_{\rm in}$ graphs are somewhat sharper in the simulation than the real data, while the shapes of the $\langle n_g \rangle$ versus $\sigma_{\rm in}$ graphs differ markedly. In addition, the percentage of total objects grouped and the mean number of objects per group is significantly higher in the real data. This could result if the real galaxies are either more strongly clustered or have smaller random velocities than those in the simulation. Our interpretation of the $\sigma_{\rm out}$-$\sigma_{\rm in}$ and related diagrams is rigorous only to the degree that the simulation precisely mimics the real universe. The differences just cited show the likeness is imperfect, and we should view our reasoning as heuristic rather than exact. There is thus larger uncertainty in our TF scatter estimate than is suggested by the previous paragraph.

Nonetheless, this uncertainty remains small. The MAT TF scatter is unlikely to be greater than the asymptotic value of 0.45–0.46 mag. Moreover, the abrupt change in slope of the $\sigma_{\rm out}$-$\sigma_{\rm in}$ diagram at $\sigma_{\rm in} \approx 0.40$ mag argues against a TF scatter less than ~0.40 mag. A generous estimate of the "total" scatter uncertainty (~95% confidence) would thus be about ±0.03 mag. A conservative estimate of the rms (~65% confidence) scatter uncertainty is about ±0.02 mag, or ~5%. This error is systematic in that it stems from our inability to state precisely which value of $\sigma_{\rm in}$ is optimal for the group calibration. The purely statistical error on the scatter (shown as the error bars in the upper right panel of Figure 5) is ~0.01 mag and is thus relatively unimportant.

A final question concerning the validity of the group TF calibration is whether the ~85% of all objects that are grouped, and thus participate in the calibration, represent a "special," low-scatter subset. One way to answer this is to carry out Hubble flow fits only to those objects that were grouped. We have done so for the output of the $\sigma_{\rm in} = 0.50$ mag

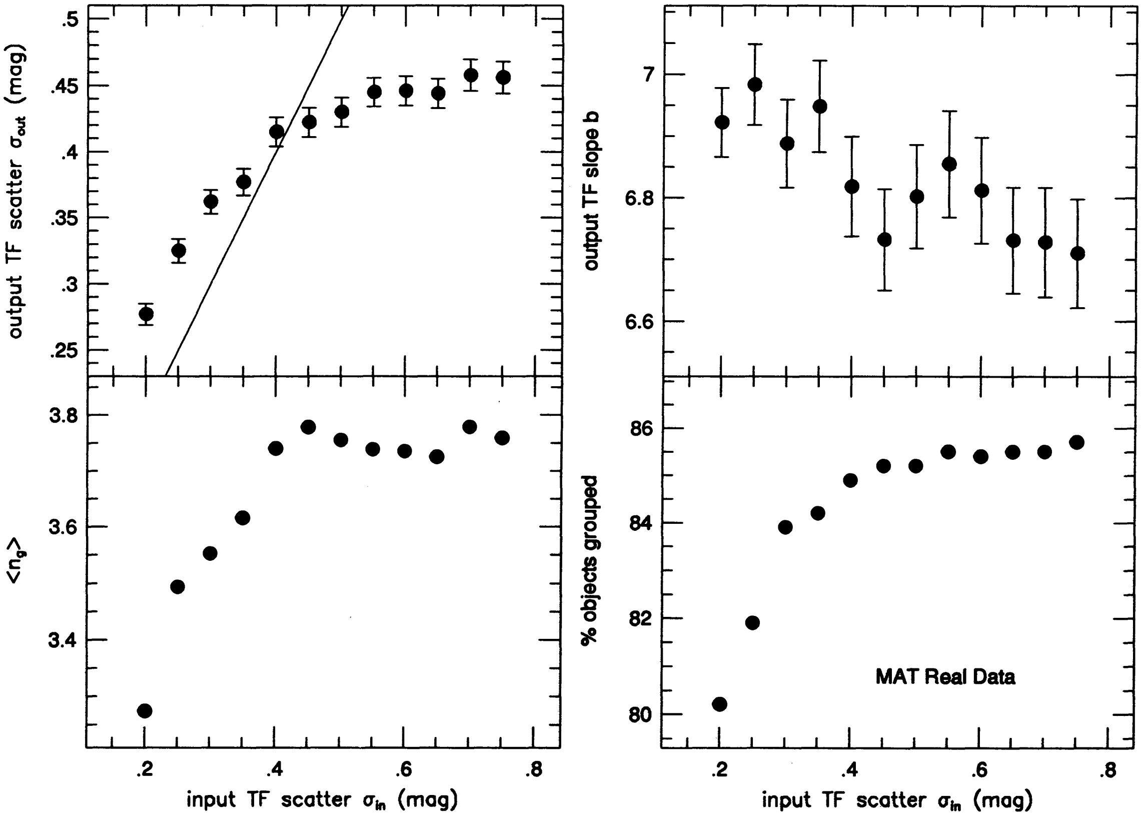

FIG. 5.—Same as Fig. 4, but results for the real MAT sample are shown

run of the grouping algorithm; the results are presented in Table 3. The numbers in the table demonstrate that there is nothing special about the TF characteristics of the grouped objects as compared with the full MAT sample. The TF parameters in Table 3 differ inconsequentially from the corresponding quantities in Table 2. The Hubble flow scatters are, if anything, somewhat larger for the grouped objects. Thus, the lower scatter ($\sim$0.43 mag) obtained by treating members of a given group as equidistant, as compared with the assumption of (heliocentric) Hubble flow ($\sim$0.47 mag), shows that the groups provide a better model of TF-orthogonal distances. This confirms the utility of the grouping algorithm as a tool for TF calibration and further validates our later use of these groups in velocity analyses.

2.2.4. *The Provisional MAT TF Relation*

We can now provide a "provisional" MAT TF relation. By this we mean the correct slope and scatter as derived from the grouping algorithm but an approximate zero point derived from the Hubble flow fit. For the slope we adopt the output of the $\sigma_{\rm in} = 0.5$ mag run of the grouping algorithm. For the scatter we adopt 0.43 mag, also the value produced by the $\sigma_{\rm in} = 0.5$ mag run but, more importantly, the mean value of $\sigma_{\rm out}$ for those runs with acceptable values of $\sigma_{\rm in}/\sigma_{\rm out}$ as suggested by the simulation. For the zero point, we adopt the value obtained from the heliocentric Hubble flow fit to the entire MAT sample (which differs negligibly from that obtained from the CMB fit). Note that this provisional zero point is, in effect, calculated the same way we calculated the final TF zero point for the HM sample in Paper I—i.e., it assumes that redshift equals distance in the mean. As we shall see at the end of this paper (§ 8), the final zero point differs relatively little from the provisional one, which indicates that the assumption that redshift equals distance is not a bad one, when averaged over the entire MAT sample. The parameters of the provisional MAT forward TF relation are presented in Table 4. Also shown in the table are the parameters of the inverse MAT TF relation, which we discuss further below. In Figure 6 we plot the MAT-sample TF relation (*left*) obtained from the $\sigma_{\rm in} = 0.5$ mag run of the grouping algorithm. The absolute magnitudes plotted are bias-corrected but are otherwise relative (i.e., they are given by $m - \mu - A$, where $\mu + A$ is the quantity actually returned by the algorithm). The line drawn through the points indicates the computed MAT TF slope. In the right panels of the figure, TF fit residuals are plotted against η and Galactic extinction A_B. No significant trends are seen, which demonstrates the validity of a linear TF relation and our adopted Galactic extinction corrections (see Paper III). In the residual-η plot there appears to be less scatter at the largest velocity widths, an effect noted by Federspiel, Sandage, & Tammann (1994). A full analysis of this effect is complicated, as the effects of the bias-correction procedure must be taken into account, and we defer further discussion of this issue to Paper III. For now, we note only that a decrease in scatter with increasing η is detectable but is small enough not to affect the calibration analysis presented here.

TABLE 3

MAT Hubble TF Relation: Grouped Objects

Reference Frame	A	b	σ (mag)	N_σ
Heliocentric	−5.831	6.793	0.472	1035
CMB	−5.837	6.817	0.504	1033
Local Group	−5.723	6.930	0.486	1034

Notes.—Parameters that result from fitting a forward TF relation to those MAT objects that were placed in groups (in the $\sigma_{\rm in} = 0.50$ mag run of the grouping algorithm). The fits were carried out under the assumption of uniform Hubble flow in heliocentric, CMB, and LG frames of reference. N_σ is the number of objects (those with fit residuals less than 1.75 mag) used in the scatter computation. In each case a total of 1040 objects participated in the fit.

TABLE 4

Parameters of the Provisional MAT TF Relations

	Forward			Inverse		
Sample	A	$b(\pm)$	σ (mag)	D	$e(\pm)$	σ_η
MAT	−5.83	6.80 (0.08)	0.43	−6.03	0.1318 (0.0016)	0.058

Notes.—Parameters of the provisional MAT forward and inverse TF relations. The slopes and scatters, which are final, were obtained from the $\sigma_{\rm in} = 0.50$ mag run of the grouping algorithm. The zero points remain to be adjusted through an overlap comparison with other samples.

2.2.5. *Physical Significance of the Hubble Flow versus Group TF Scatter*

The difference between the heliocentric Hubble flow scatter (0.47 mag) and the grouping-algorithm output scatter (0.43 mag) most likely reflects the radial peculiar motions of sample galaxies. The indicated motions are on the order of $\sim(\ln 10/5)(0.47^2 - 0.43^2)^{1/2} \approx 9\%$ of the typical object distances. The effective depth of the MAT sample is $\sim$2500–3000 km s^{-1}. Thus, the typical radial peculiar motions have amplitude $\sim$250 km s^{-1}. In making this rough calculation, we have used the Hubble flow scatter in a *heliocentric* frame. The fact that the Hubble flow scatter in the CMB frame is significantly larger indicates that, in addition to these small-scale motions, there is a large-scale component to the flow field shared by much of the sample. In later papers in this series we will study these issues in detail.

2.2.6. *An Inverse TF Relation for MAT*

As we did in Paper I for HM and W91CL, we derive an inverse TF relation for MAT. The rationale is twofold: first, the comparatively unbiased character of an inverse TF fit enables a check (see below) on the significant bias corrections applied in the forward calibration; second, the inverse relation is useful in its own right for later peculiar velocity studies. In Paper I, we noted that even the inverse fits required small bias corrections for HM and W91CL because of the η-dependence in the relationship between the TF magnitudes and certain of the selection quantities. The inverse TF fit for the MAT sample requires no bias correction analogous to that done for HM and W91CL because the log $D_{\rm ESO}$–m_I relation was found to be η-dependent. However, we have imposed a strict lower limit of $\eta = -0.42$ in defining our calibration sample (see above). In what follows, we implement the W94 bias-correction procedure appropriate to this strict η-limit. In practice, relatively few galaxies have small η-values near the limit, and thus the effect of this correction on the inverse TF fit is small.

We fit to the groups formed by the preferred $\sigma_{\rm in} = 0.50$ mag run of the grouping algorithm. The inverse relation is taken to be of the form $\eta^0(M) = -e(M - D)$, and its scatter is denoted σ_η (see Paper I). The method of fit is exactly as described in § 3.3.1 of Paper I (except, of course, that none of the present groups are allowed to "expand" in the Hubble flow). The slope e and

1996ApJ...457..460W

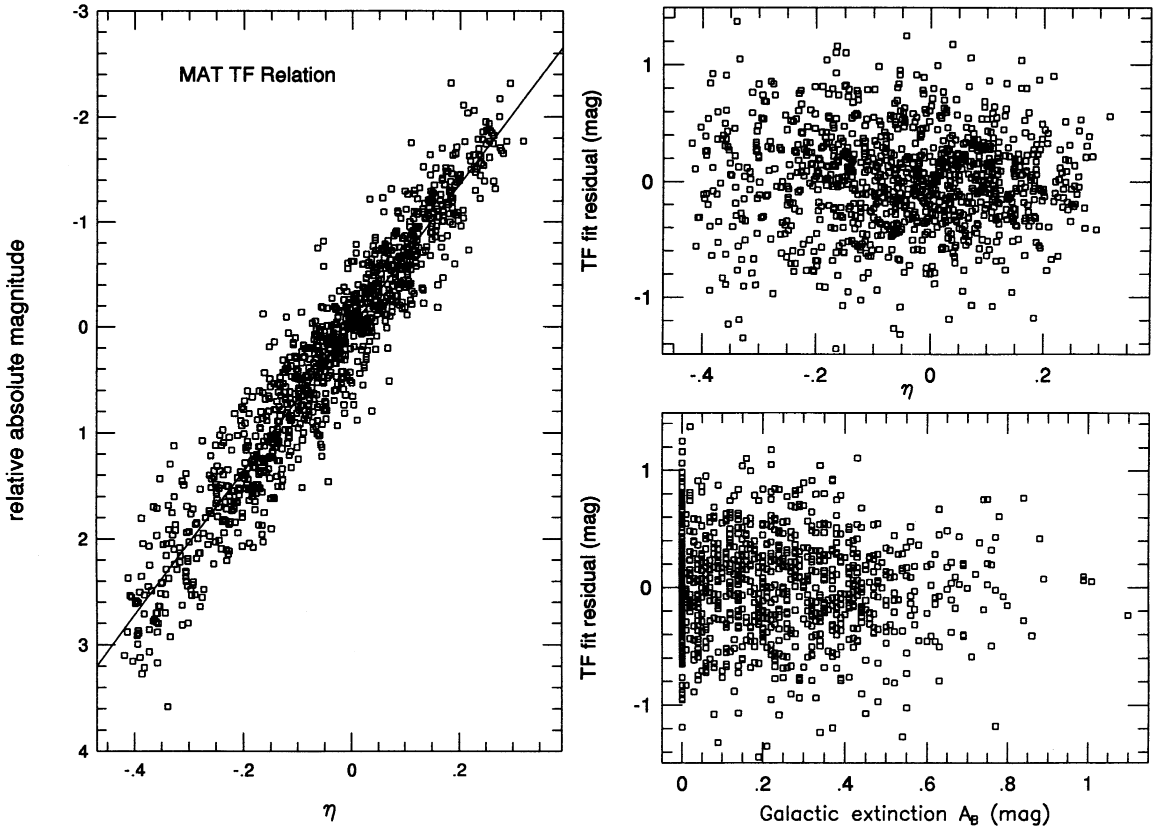

FIG. 6.—*Left:* MAT-sample TF relation, obtained from the groups formed by the $\sigma_{\rm in} = 0.50$ mag run of the grouping algorithm. The solid line drawn through the points shows the fitted slope of 6.80. The absolute magnitudes plotted are relative only, as a final zero point has yet to be assigned to the MAT TF relation. *Right:* Residuals from this TF relation with respect to η (*top*) and the *B*-band Galactic extinction A_B (*bottom*). All plots are corrected for selection-bias effects.

scatter σ_n obtained from this fit are presented in Table 4. The zero point *D* was calculated by fitting an inverse TF relation to the MAT sample using the heliocentric Hubble flow model. Like its forward counterpart *A*, this zero point is provisional only, pending the overlap analysis in § 6.

2.2.7. *Validating the Bias Corrections: Comparison of the Forward and Inverse Fits*

As in Paper I, we address the validity of the selection-bias corrections by comparing distance moduli from the forward and inverse TF fits. To review briefly the rationale behind this comparison,[9] the inverse TF fits experience small or no bias, whereas the forward TF fits suffer large selection bias. One manifestation of the bias is that distances are compressed, with the most biased (in general, the most distant) groups appearing closer than they actually are. Consequently, a plot of forward minus inverse group distance modulus versus redshift should reveal a trend for a "naive" forward TF fit; when the forward fit has undergone a proper bias-correction procedure, no such trend should be evinced.

Figure 7 shows the difference between forward and inverse group distance moduli as a function of log redshift for MAT groups of four or more members. In the upper panel, the forward moduli obtained prior to the application of the W94 bias-correction procedure are used; in the lower panel, the fully corrected forward moduli are used. (In each panel, the modulus differences are adjusted so that their mean value vanishes; as we have not yet finalized either the forward or inverse TF calibrations, this shift is unimportant.) The top panel reveals the effects of selection bias: there is a systematic trend with increasing redshift, in the sense that more distant (higher redshift) groups have their distances underestimated by the forward TF fit. A linear fit of $[\mu(\text{forw}) - \mu(\text{inv})]$ to log *cz* yields a slope of -0.484 ± 0.048, which indicates that the trend is highly significant. The lower panel demonstrates the efficacy of the bias-correction procedure. The strong trend seen in the top panel is gone; a linear fit of $[\mu(\text{forw}) - \mu(\text{inv})]$ to log *cz* now yields a slope of 0.059 ± 0.048, which is not statistically significant. As in Paper I, we took the error bars on the modulus differences to be $\propto n^{-1/2}$, where n was the number of objects in a group, and adjusted the coefficient of this factor so that the χ^2 of the linear fit took on its expected value of $N - 2$, where N was the total number of groups used in the fit.

2.3. *Determination of the MAT Internal-Extinction Coefficient*

In Paper I, we estimated the internal-extinction coefficients ($C_{\rm int}$) for the HM and W91CL samples by minimizing TF scatter. Because $C_{\rm int}$ should depend only on photometric bandpass, the *I*-band MAT and HM samples should in principle have the same internal-extinction coefficient $C^I_{\rm int}$. In fact, the preceding TF analysis was carried out with $C^I_{\rm int} = 0.95$. Here we verify that this choice was the correct one by examining the MAT TF scatter with respect to $C^I_{\rm int}$.

We have done this test using two separate fits: the preferred $\sigma_{\rm in} = 0.5$ mag run of the grouping algorithm and a heliocentric Hubble flow fit. In the former, we did not change the groups originally formed, simply refitting a TF relation to those

---

[9] A more detailed discussion is provided in Paper I, § 5.1.

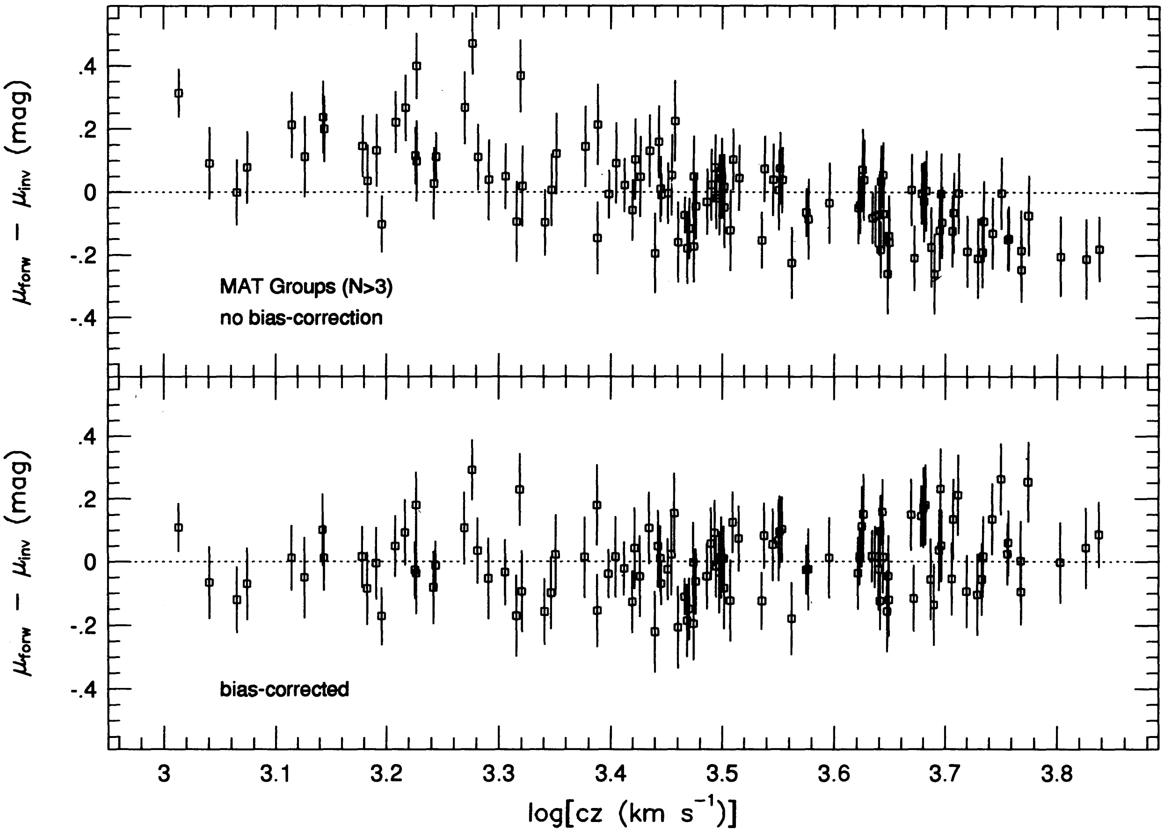

FIG. 7.—The difference between forward and inverse group-distance moduli obtained from the TF calibration fit, for MAT groups with four or more members. In the top panel the forward distance moduli have not been corrected for selection bias; in the bottom panel they have been. The trend in the upper panel is characteristic of selection bias; the lack of a trend in the lower panel indicates the success of the bias-correction procedure.

groups for a range of values of $C^I_{\rm int}$. This approach suffers from the possible objection that, since a particular value of $C^I_{\rm int}$ (namely, 0.95) was built into the group-forming procedure, that value is preferred by the TF relation fitted to the groups. With the Hubble flow fits, there is no such objection. However, the inherent scatter of the Hubble flow fit is larger, which could diminish the discriminatory power of the test.

The left panel of Figure 8 shows how the TF scatter for the two kinds of fits varies as a function of internal-extinction coefficient. It is evident that the Hubble flow and group scatters vary with $C^I_{\rm int}$ in a very similar way; both curves reach a minimum at $C^I_{\rm int} \lesssim 1$. The value $C^I_{\rm int} = 0.95$ is consistent with either the Hubble flow or the group fit. According to the argument of Paper I (§ 3.2.3), a 65% confidence interval occurs when the quantity $N_{\rm eff}\sigma^2$ changes by one unit. For the group fit, $N_{\rm eff} = 758$ (total objects grouped minus number of groups formed minus 1 for the fitted slope) while for the Hubble flow fit $N_{\rm eff} = N_\sigma - 2$, where $N_\sigma = 1209$ (Table 2). We plot as dotted lines the corresponding values of σ. These show that with ~65% confidence $0.75 \lesssim C^I_{\rm int} \lesssim 1.15$. These limits are similar to, but tighter than, those derived from the HM sample (see Paper I, § 3.2.3), for which we found $0.65 \lesssim C^I_{\rm int} \lesssim 1.30$ with 65% confidence. The fact that the two samples are in excellent agreement gives us further confidence in our adopted value of $C^I_{\rm int} = 0.95$.

In the right panels of Figure 8 we plot TF residuals versus log axial ratio, for fits to the $\sigma_{\rm in} = 0.50$ mag groups, using our final adopted value of $C^I_{\rm int} = 0.95$. The upper right panel shows forward TF fit residuals (bias-corrected observed apparent magnitude minus expected apparent magnitude $\mu + A - b\eta$). There is no trend with axial ratio. This is to be expected since we have chosen $C^I_{\rm int}$ to minimize the forward TF scatter. The lower right panel shows inverse TF fit residuals (observed minus predicted value of η). Again, no trend of the residuals with axial ratio is apparent. This is important because we did not use the inverse TF scatter to constrain $C^I_{\rm int}$. In addition, since the inverse fit is essentially unbiased, there can be no "cross talk" between the bias-correction procedure (which is axial-ratio dependent) and the internal-extinction correction. The fact that inverse TF residuals exhibit no trend with axial ratio thus further confirms the validity of our adopted value of $C^I_{\rm int}$.

2.3.1. *A Luminosity Dependence of Internal Extinction?*

In this series of papers, we assume that the internal-extinction correction depends on axial ratio only (see Paper I, § 2). However, it has recently been claimed (Giovanelli 1995) that $C^I_{\rm int}$ increases with luminosity, rising from a value of ~0.5 for the least luminous galaxies to ~1.3 for the most luminous objects. It has been further argued that application of a luminosity-dependent extinction correction has important consequences for the local peculiar velocity field (Giovanelli et al. 1995). Here we investigate the validity of this claim using the MAT sample, by testing whether the TF residuals indicate that luminous galaxies are undercorrected, and faint galaxies overcorrected, for internal extinction.

While Giovanelli (1995) described a dependence on luminosity, any test involving fit residuals must consider a depen-

1996ApJ...457..460W

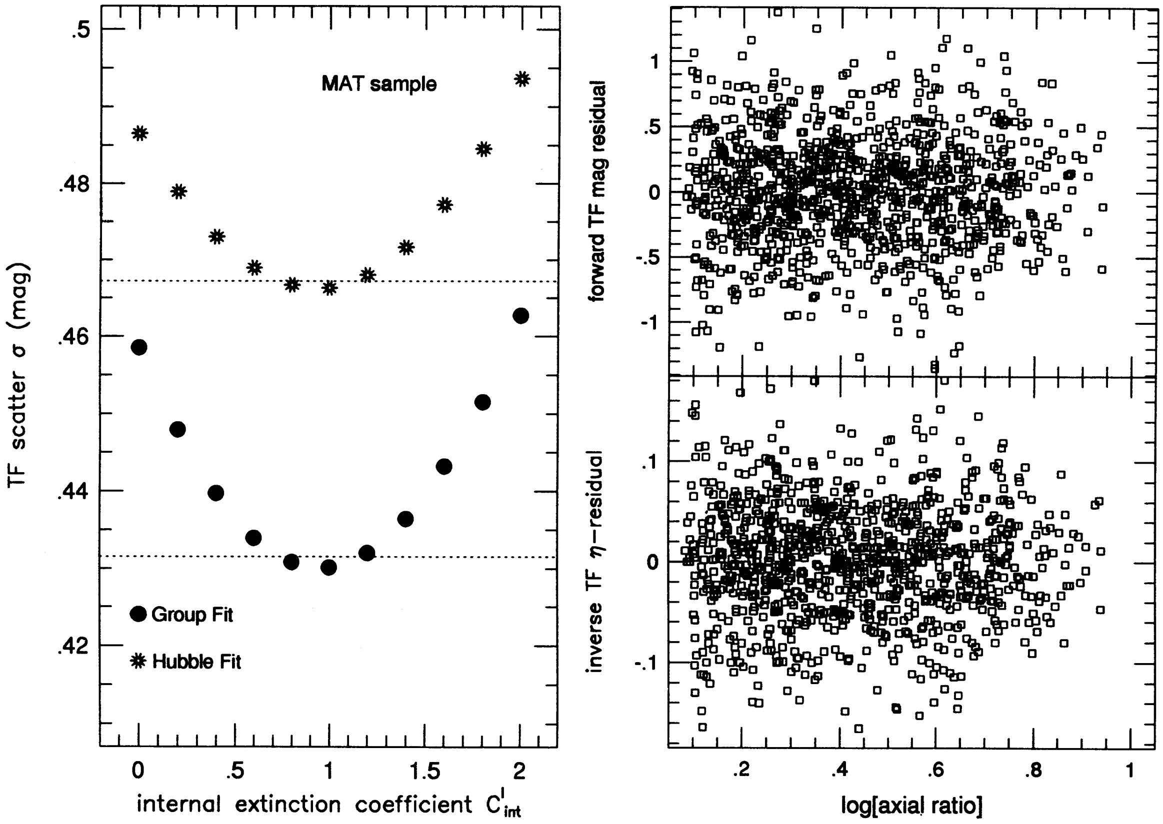

FIG. 8.—*Left:* TF scatter plotted as a function of the I-band internal-extinction coefficient for the MAT sample. Results for both a heliocentric Hubble flow fit and a fit to the $\sigma_{\rm in} = 0.50$ mag groups are shown. In each case a 65% confidence interval on $C^I_{\rm int}$ is given by the intersection of the points with the horizontal dotted line. *Right:* TF residuals plotted against log axial ratio for the $\sigma_{\rm in} = 0.50$ mag group fit, using the final adopted value $C^I_{\rm int} = 0.95$. Forward (*top*) and inverse (*bottom*) TF residuals are shown.

dence only on the independent variable in the fit. Because luminosity (via the apparent magnitude) is the *dependent* variable in the forward TF fit, we must search instead for an η-dependence of internal extinction when we consider forward-fit residuals. To search for a dependence on luminosity per se, we must use residuals from the inverse fit. We present both of these tests in what follows.

To carry out the test using forward TF residuals, let us suppose that the internal-extinction coefficient should properly be written

$$C^I_{\rm int}(\eta) = C^I_{{\rm int},0} + g_f\,\eta\,, \qquad (4)$$

where $C^I_{{\rm int},0}$ is the mean I-band extinction coefficient, and g_f measures the increasing strength of internal extinction with increasing velocity width. (The subscript f denotes "forward.") Giovanelli (1995) did not formulate the luminosity dependence of internal extinction according to our equation (4) (see his Fig. 2*c*), but our formulation is consistent with the data points he shows. Specifically, his Figure 2*c* indicates a change of ~0.85 in $C^I_{\rm int}$ over an interval of ~5.8 in absolute magnitude. The corresponding value of g_f is thus $g_f \approx (0.85/5.8)b_{\rm TF} \approx 1$, where $b_{\rm TF} = 6.8$ is the slope of the forward MAT TF relation.

Neglect of a possible luminosity (velocity width) dependence of internal extinction corresponds to the assumption $g_f \equiv 0$. If this assumption is wrong, then the apparent magnitudes we have used in our TF fits above are also wrong. In particular, our forward TF fits should exhibit apparent magnitude residuals (observed minus predicted) given by $\delta m = g_f\,\eta\mathscr{R}$, where $\mathscr{R}$ is the logarithm of the (major to minor) axial ratio (see Paper I). In the upper panel of Figure 9, we plot forward TF residuals versus the product $\eta\mathscr{R}$ for the output of the preferred $\sigma_{\rm in} = 0.5$ mag run of the grouping algorithm. The left side of the plot corresponds to faint (low η), inclined (large $\mathscr{R}$) galaxies, while the right side corresponds to bright, inclined galaxies. Objects that populate the center of the plot are of ordinary luminosity ($\eta \sim 0$) or very low inclination. We have superposed a dashed line corresponding to $g_f = 1$, which shows how the residuals would behave if Giovanelli's effect were present. The residuals do not follow the dashed line. In fact, carrying out a linear fit of the TF residuals to the product $\eta\mathscr{R}$, we obtain a slope of -0.22 ± 0.17, which is consistent with the visual impression that there is no significant trend in the plot. From the forward TF residual test we cannot detect an η-dependence of the coefficient of internal extinction.

It is useful to carry out the same test with the inverse TF fit as well, for two reasons. First, the inverse fit is independent of the bias-correction procedure; second, as noted above, it enables us to test for a luminosity dependence *directly*, rather than indirectly through the M-η correlation. To make this test, we suppose the internal-extinction coefficient should be written

$$C^I_{\rm int}(M) = C^I_{{\rm int},0} - g(M-D)\,, \qquad (5)$$

where $g > 0$ implies an increase in internal extinction with increasing luminosity (the absence of the subscript f used above now implies the appropriate formulation for the inverse TF residual test). In equation (5) we have "normalized" the abso-

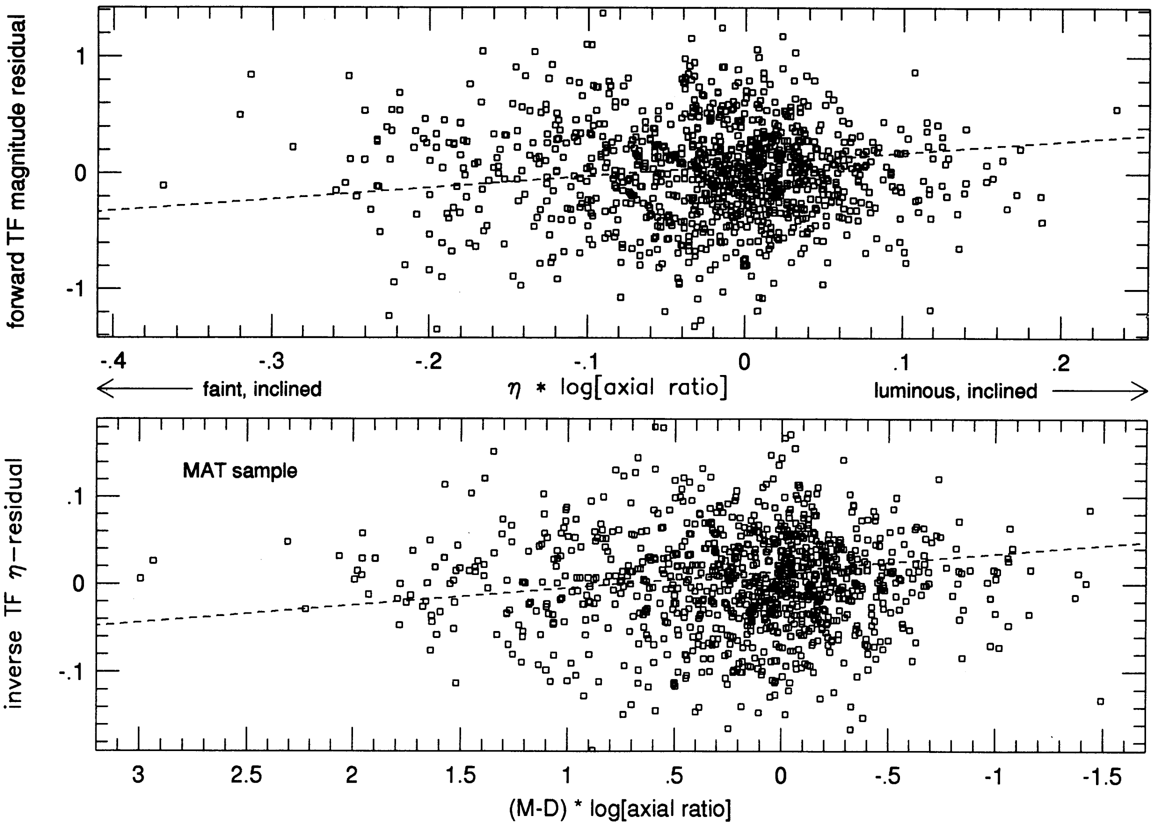

FIG. 9.—MAT-sample TF residuals, for the $\sigma_{\rm in} = 0.50$ mag group fit, plotted against quantities that test for a luminosity dependence of internal extinction. In the upper panel, forward TF residuals are plotted against the product $\eta\mathscr{R}$ (where $\mathscr{R}$ = log axial ratio). In the lower panel, inverse TF residuals are plotted against the product $(M-D)\mathscr{R}$, where M is absolute magnitude and D is the inverse TF zero point. The dashed lines drawn through the points show the expected trend of the residuals according to the luminosity dependence of internal extinction proposed by Giovanelli (1995). As discussed in the § 2.3.1, the residuals do not follow this trend, which indicates the absence of such a dependence.

lute magnitude dependence by the inverse TF zero point D so as to facilitate comparison with the forward case (note that $M = D$ corresponds to $\eta = 0$).

Our neglect of the luminosity dependence (i.e., our assumption that $g \equiv 0$) implies that our inverse TF fit should exhibit η-residuals given by $\delta\eta = -e_{\rm TF}\, g(M-D)\mathscr{R}$, where $e_{\rm TF}$ is the inverse TF slope. Thus, a plot of $\delta\eta$ versus the product $(M-D)\mathscr{R}$ should have a slope of $e_{\rm TF}\, g$. The value of g implied by Figure 2*c* of Giovanelli (1995) is $g \approx 0.85/5.8 = 0.147$; using the MAT inverse TF slope from Table 4, we find that this slope should be ~ 0.02 if Giovanelli's effect is real. In the lower panel of Figure 9, we plot TF η-residuals versus $(M-D)\mathscr{R}$ for the preferred $\sigma_{\rm in} = 0.5$ mag run of the grouping algorithm. Superposed on the plot is a dashed line of slope 0.02. As in the forward case, the points do not follow the dashed line. When we carry out a linear fit of the inverse TF residuals to the product $(M-D)\mathscr{R}$, we obtain a slope of 0.001 ± 0.003, which verifies the visual impression that the η-residuals exhibit no significant correlation with the product $(M-D)\mathscr{R}$. Thus, the inverse TF residual test confirms the result found from its forward counterpart: there is no evidence in the MAT-sample data for a variation of internal-extinction coefficient with galaxy luminosity.

3. THE W91PP SAMPLE

The TF sample of Willick (1991) consists of cluster and field subsamples. In Paper I, we treated the cluster subsample (W91CL); here we study the field subsample, which we refer to as W91PP because its members are located in the Perseus-Pisces (P-P) filament. The full W91PP sample consists of 385 galaxies in the densest part of the P-P supercluster, centered on $l \sim 120°$, $b \sim -30°$. For reasons we describe further below, in this and later papers we use only a 326 galaxy subsample. W91PP is drawn from a larger sample of galaxies in P-P with H I measurements from Giovanelli, Haynes, and coworkers (Giovanelli & Haynes 1985; Giovanelli et al. 1986a, b; Giovanelli & Haynes 1989; hereafter, collectively, GH). Details of the selection of objects from GH are given by Willick (1991). The photometric characteristics of W91PP are identical to those of W91CL, which are discussed in Paper I. The raw velocity widths used for W91CL are the 20% H I line widths, ΔV_{20}, published by Aaronson et al. (1986), whereas the widths published by GH are 50% line widths, ΔV_{50}. Willick (1991) derived a conversion between ΔV_{50} and ΔV_{20} (the formula applies to raw widths and therefore is unaffected by the inclination correction), and all of the GH 50% widths have been converted into equivalent 20% widths for the analysis presented here. The W91CL and W91PP η-systems should thus in principle be equivalent, but there is no guarantee that this is so in practice. As we shall see, the W91PP TF relation is considerably flatter than the W91CL TF relation (Paper I), which may be the result of a systematic difference between their respective η-systems. For this reason, we will independently derive a TF relation for W91PP, treating it, in effect, as a separate sample.

TABLE 5

W91PP TF Relation from Hubble Flow Fits

Reference Frame	A	b	σ (mag)	N_σ
Heliocentric.......	−4.168	6.926	0.414	326
CMB	−4.002	7.107	0.420	324
Local Group......	−4.284	6.813	0.410	326

Notes.—Parameters that result from fitting a forward TF relation to the W91PP sample, under the assumption of uniform Hubble flow in a heliocentric, CMB, and LG frame of reference. N_σ is the number of objects (those with fit residuals less than 1.5 mag) used in the scatter computation. In each case a total of 326 objects participated in the fit.

To calibrate the W91PP TF relation, we must first quantitatively characterize the sample-selection criteria. The H I data compilations of GH claimed completeness roughly to the limit of the UGC but not of the Zwicky (Zwicky et al. 1961–1968) catalog.[10] We have eliminated the ∼60 "Zwicky only" galaxies included in the original list of Willick (1991). The remaining 326 galaxies are all UGC objects, and the sample is thus roughly complete to the UGC limiting diameter of 1′. The W91PP TF calibration will thus use the "one catalog" selection formulae of W94. However, to account for incompleteness near the catalog limit, we have set the formal diameter limit in the bias-correction algorithm to 1′.15; we will justify this choice later, when we compare results from the forward and inverse TF fits. The coefficients of the linear relation between the logarithmic UGC diameter and the TF observables are those given in Table 5 of Paper I. Like the W91CL sample (Paper I), the velocity widths for W91PP were obtained from Arecibo, and incompleteness associated with H I nondetection may be neglected. However, the selection of objects from the GH compilation by Willick (1991) included the requirement $\Delta V_{50} \geq 200$ km s^{-1}, which implies $\eta \geq -0.2$. We will take this into account in the inverse TF fit (§ 3.1.4).

3.1. *Calibration of the W91PP TF Relation*

Like the MAT sample, W91PP is suitable for application of the redshift-space grouping algorithm (§ 2.2.2). Grouping of W91PP is particularly important for the later velocity analysis because of the strong density gradients in the P-P region and consequent susceptibility to inhomogeneous Malmquist bias. Here we use the groups as the basis of the W91PP TF calibration.

3.1.1. *Preliminary Hubble Flow Fits*

A preliminary TF calibration for W91PP is obtained from Hubble flow fits, carried out exactly as for MAT (§ 2.2.1). Table 5 shows the results of such fits. The scatter is rather insensitive to reference frame (although it is noteworthy that, as with MAT, the CMB frame does not provide the best fit). As before, we may view the best-fit scatter of ∼0.41 mag as an upper limit; the true W91PP TF scatter is smaller to the degree the Hubble flow model is imperfect. The TF zero points obtained in the various frames are reasonably similar to the provisional W91CL TF zero point obtained in Paper I. However, the slopes in any frame are noticeably smaller than the value $b \approx 7.7 \pm 0.2$ derived for W91CL. We defer a full discussion of this point until later, pending the outcome of the group analysis.

We use the preliminary TF parameters from the heliocentric Hubble flow fit as input to the grouping algorithm. We apply the algorithm both to the real W91PP sample and to the simulated W91PP sample from Kolatt (1995) for a range of input scatters. The goal again is to constrain the W91PP scatter from the appearance of the $\sigma_{\rm out}$-$\sigma_{\rm in}$ diagram, using the simulation as a guide. The simulated W91PP sample followed a TF relation of slope 7.35 and scatter 0.37 mag and had selection criteria comparable to those of the real sample. The best Hubble flow fit to the simulated sample had a scatter of 0.41 mag.

In Figure 10 we show the results of applying the grouping algorithm to the simulated W91PP sample. As we saw for the simulated MAT sample (§ 2.2.3), $\sigma_{\rm out}$ is equal within the statistical errors to the true TF scatter when $0.95 \lesssim \sigma_{\rm in}/\sigma_{\rm out} \lesssim 1.25$. For $\sigma_{\rm in} \gtrsim 0.50$ mag, $\sigma_{\rm out}$ significantly exceeds the true scatter, although it asymptotes to ∼0.39 mag, less than the Hubble flow scatter. The lower right panel of Figure 10 reinforces the principle derived from the simulated MAT sample, namely, that the correct value of the output scatter occurs when the percentage of objects grouped is in the plateau region of its characteristic curve. The upper right panel of the figure shows that the fitted TF slopes are statistically consistent with the correct value and manifest no systematic trend.

In Figure 11, we show the results of applying the grouping algorithm to the real W91PP sample. The various panels of the figure resemble their counterparts in Figure 10 well enough that we may trust the latter as an interpretive guide. We thus find that the correct value of $\sigma_{\rm in}$ is in the range 0.35–0.45 mag; the correct TF scatter corresponds to the values of $\sigma_{\rm out}$ for those runs, i.e., $\sigma = 0.38 \pm 0.01$ mag. However, from statistical considerations alone the scatter uncertainty is ∼0.018 mag. As this statistical error is now (in contrast with the case of the MAT sample) larger than the systematic error associated with locating the proper value of $\sigma_{\rm in}$, the actual rms scatter uncertainty is not much larger than the statistical error, and we estimate it to be ∼0.02 mag, the same as for MAT. The output scatter asymptotes to $\lesssim$0.40 mag, somewhat less than the Hubble flow scatter.

As we did with MAT, we have also carried out Hubble flow fits for the grouped objects only. The resulting TF parameters were essentially unchanged from those obtained with the full sample, with a marginally lower best-fit scatter (0.403 mag). This verifies that the lower scatter (0.38 mag) obtained from fitting a TF relation to the grouped objects does not result from picking out a smaller scatter subsample, but from the fact that the redshift-space groups constitute a better TF-orthogonal distance model than Hubble flow.

3.1.2. *The Provisional W91PP TF Relation*

For our provisional forward W91PP TF relation, we adopt the slope and scatter obtained from the $\sigma_{\rm in} = 0.40$ mag run of the grouping algorithm. For the provisional TF zero point, we adopt the value obtained from the LG-frame (smallest scatter) Hubble flow fit to the full sample. The parameters of this provisional TF relation are given in the three columns of Table 6 labeled "Forward." Also shown are the parameters of the provisional inverse TF relation for W91PP, which we discuss below (§ 3.1.4).

In the left panel of Figure 12 we plot the W91PP TF relation obtained from the $\sigma_{\rm in} = 0.40$ mag run of the grouping algorithm. Again, relative absolute magnitudes $(m - \mu - A)$ are plotted, as a final zero point has not yet been assigned. The solid line drawn through the points is the TF slope fitted to the

---

[10] More recent work the Giovanelli/Haynes group remedies this incompleteness, but W91PP does not reflect these recent additions.

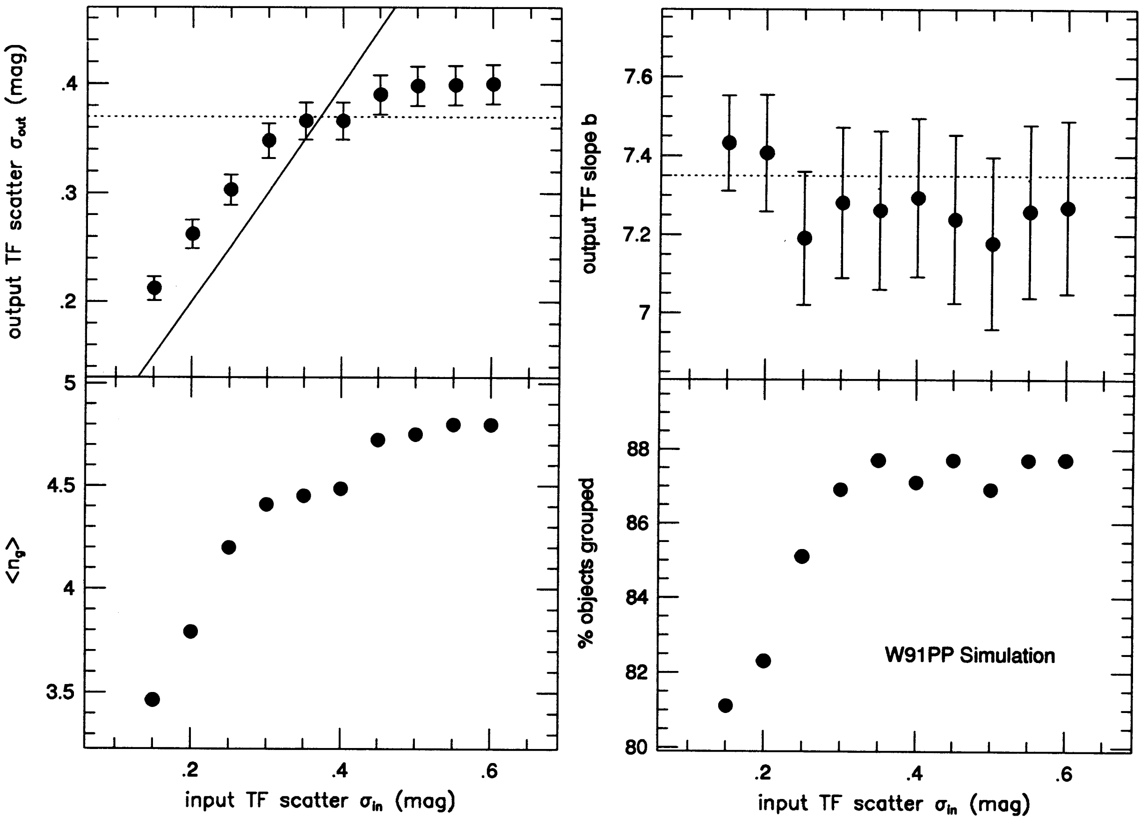

FIG. 10.—Same as Fig. 4, but results for the simulated W91PP sample are now shown

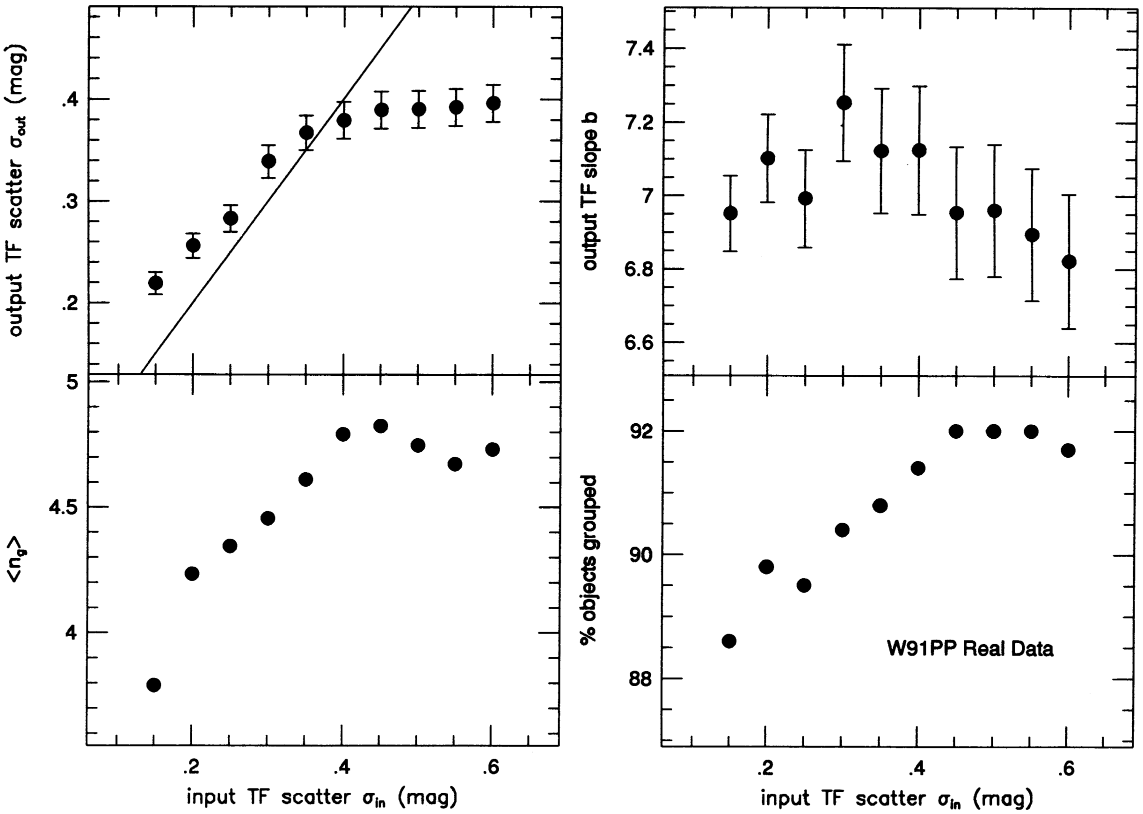

FIG. 11.—Same as Fig. 4, but results for the real W91PP sample are now shown

1996ApJ...457..460W

TABLE 6

PARAMETERS OF THE PROVISIONAL W91PP TF RELATIONS

	FORWARD			INVERSE		
SAMPLE	A	$b\,(\pm)$	σ (mag)	D	$e\,(\pm)$	σ_η
W91PP......	−4.28	7.12 (0.18)	0.38	−4.36	0.1244 (0.0031)	0.049

NOTES.—Parameters of the provisional W91PP forward and inverse TF relations. The slopes and scatters, which are final, were obtained from the $\sigma_{\rm in} = 0.40$ mag run of the grouping algorithm. The zero points remain to be adjusted through an overlap comparison with other samples.

groups ($b = 7.12$); the dotted line shows the slope of the W91CL TF relation derived in Paper I. Note that the two slopes describe the data more or less equally well for $-0.2 \lesssim \eta \lesssim 0.2$ (indeed, the steeper W91CL slope may be somewhat better for the lowest velocity width objects). However, for $\eta \gtrsim 0.25$, the flatter W91PP slope is clearly superior. This shows that it is valid to assign a TF slope to W91PP distinct from the one derived for W91CL. The adoption of a quadratic TF relation would allow both W91 subsamples to be consistently described by a single TF relation. However, none of the other samples, including the very large MAT sample, show evidence for a quadratic relation. We have thus opted for the simpler approach of using distinct, linear TF relations for each sample.

The right panels of Figure 12 show the W91PP TF residuals with respect to η (*top*) and A_B (*bottom*). There is no global trend with respect to η, which indicates the adequacy of the linear relation. It is remarkable that one extremely high velocity width object (UGC 12591, with $\eta = 0.528$, corresponding to a rotation velocity of 533 km s^{-1}; see Giovanelli et al. 1986) shows no significant deviation from the TF relation followed by galaxies with ordinary rotation speeds. The absence of any meaningful trend in the bottom right panel validates our adopted Galactic extinction corrections.

3.1.3. *Physical Significance of the Hubble Flow versus Group TF Scatter*

As with MAT, we may interpret the difference between the Hubble flow and group TF scatters as a measure of typical radial peculiar velocities. We use the best-fit Hubble flow scatter for the grouped objects only, as the Hubble flow scatter for the full sample was somewhat inflated due to nearby, relatively large residual points that were not grouped. We find that rms radial peculiar velocities are then given by $\sim$(ln 10/5)$(0.40^2 - 0.38^2)^{1/2}$5000 km s$^{-1} \approx$ 300 km s^{-1}, where we have taken 5000 km s^{-1} as the effective depth of the W91PP sample. This value is consistent with that found from an analogous calculation with the MAT sample (§ 2.2.5). As with MAT, the CMB frame did not provide the best Hubble flow fit (although for W91PP the differences were slight), suggesting that these rms radial motions are superposed on large-scale streaming that encompasses much of the W91PP sample.

3.1.4. *An Inverse TF Relation for W91PP*

We fit an inverse TF relation to the W91PP sample using the groups formed by the $\sigma_{\rm in} = 0.40$ mag run of the grouping

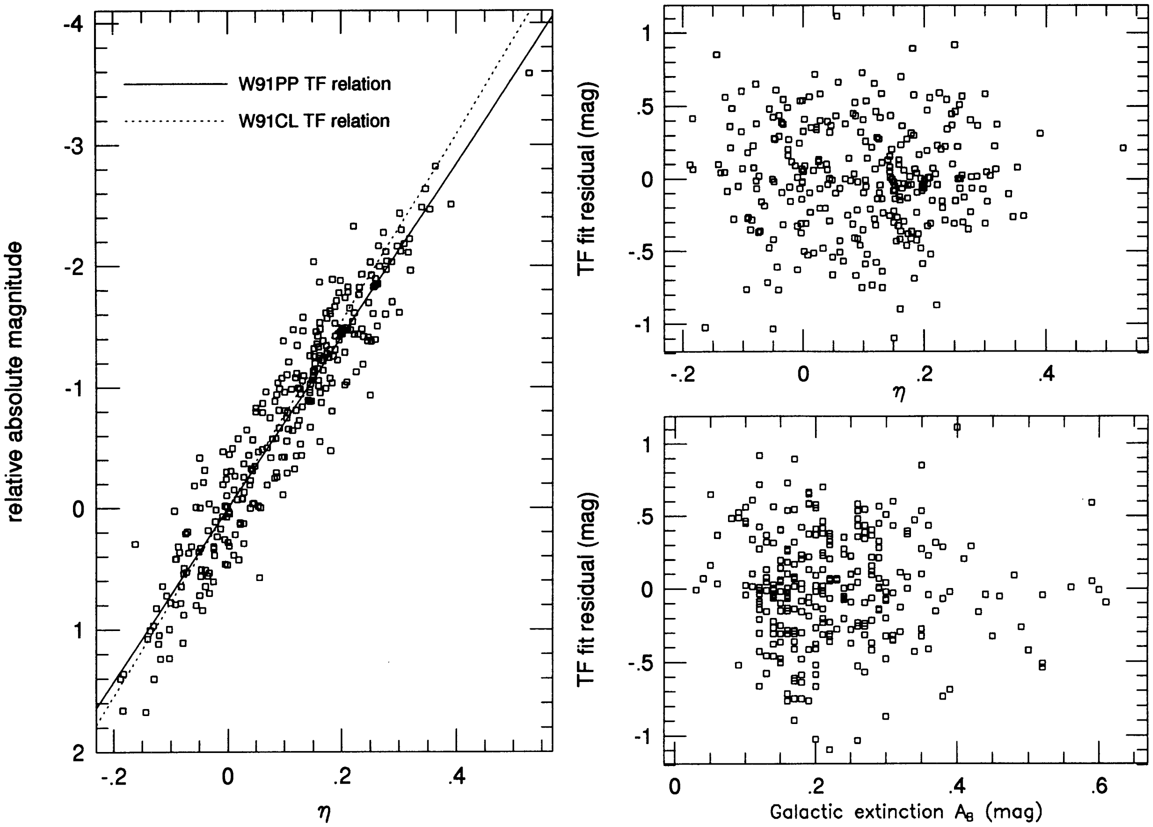

FIG. 12.—*Left:* W91PP TF relation fitted to the $\sigma_{\rm in} = 0.40$ mag groups. The solid line plotted through the points shows the fitted slope of 7.12. The dotted line shows the W91CL slope of 7.73. *Right:* The upper panel shows residuals from the fit with respect to η, and the lower panel residuals from the fit with respect to Galactic extinction A_B. All plots are corrected for selection-bias effects.

1996ApJ...457..460W

algorithm. The results are given in the rightmost columns of Table 6. The zero point was obtained from an inverse TF LG-frame Hubble flow fit. For W91PP, it was necessary to apply the W94 bias-correction procedure not only to account for the $\eta \geq -0.2$ requirement (an analogous correction was performed in the MAT inverse fit) but also for the η-dependence of the log $D_{\rm UGC}$–(m_r, η) relation (see Table 5 of Paper I).

The inverse TF slope in Table 6 differs from the inverse TF slope found in Paper I for W91CL. The sense of the difference is that expected from the difference in the forward slopes: $e_{\rm W91PP}^{-1} < e_{\rm W91CL}^{-1}$. The discrepancy between inverse slopes is somewhat smaller than that between the forward slopes. Nonetheless, the fact that the differences are in the same sense suggests that the W91PP versus W91CL slope difference is a real effect, not an artifact of the bias-correction procedure. This further supports our decision to treat W91PP and W91CL as independent samples.

3.1.5. *Validating the Bias Corrections*

In Figure 13 we plot forward-minus-inverse TF group distance moduli versus log redshift, both prior to (*top*) and after (*bottom*) application of the bias-correction procedure. As we saw with the MAT groups, the W91PP groups show clear evidence of selection bias. Prior to the bias corrections, the forward TF fit results in systematically underestimated distance moduli at larger redshifts. A linear fit of $[\mu(\text{forw}) - \mu(\text{inv})]$ to log *cz* for the uncorrected moduli yields a slope of -0.881 ± 0.115, indicating that the trend is significant. A linear fit for the corrected moduli yields a slope of -0.101 ± 0.106, i.e., no significant trend. Thus, the forward-minus-inverse distance-modulus test reveals the principle effects of selection bias and shows that the W94 bias-correction procedure removes these effects for W91PP. This error bars shown were calculated in the same way as for the MAT sample.

3.2. *Determination of the W91PP Internal-Extinction Coefficient*

We determine the extinction coefficient for W91PP exactly as we did for MAT. In the left panel of Figure 14 we plot the variation in TF scatter with the *r*-band internal-extinction coefficient $C_{\rm int}^r$, for both the heliocentric Hubble flow and group ($\sigma_{\rm in} = 0.40$ mag) fits. The two curves are in good agreement, each reaching a minimum for $C_{\rm int}^r \approx 0.80$. We exhibit a 65% confidence interval for $C_{\rm int}^r$ as a dotted line for both fits. Again, the Hubble flow fit, despite its larger scatter, is seen to place slightly tighter constraints on $C_{\rm int}^r$. The 65% confidence interval corresponds to $0.45 \lesssim C_{\rm int}^r \lesssim 1.15$. This may be compared with the range $0.65 \lesssim C_{\rm int}^r \lesssim 1.75$ found with the W91CL sample (Paper I, § 4.2.1). These ranges overlap, although their centers are offset by about 1 σ. There is thus no statistically significant discrepancy between the two samples, although we lack the remarkable agreement found between HM and MAT for the *I* band. The question then arises of what value $C_{\rm int}^r$ to adopt, finally, for the Mark III catalog. The simplest approach is to take a weighted average of the values favored by W91PP and W91CL. If the weights are given by the effective number of degrees of freedom in the fits, we obtain our final result, $C_{\rm int}^r = 0.95$, the value used in the TF analysis above. The right panels of Figure 14 show forward (*top*) and inverse (*bottom*) TF residuals, plotted as a function of log axial ratio, that result from the fit to the $\sigma_{\rm in} = 0.40$ mag W91PP groups. There is no trend evident in either panel. As we argued in the case of the

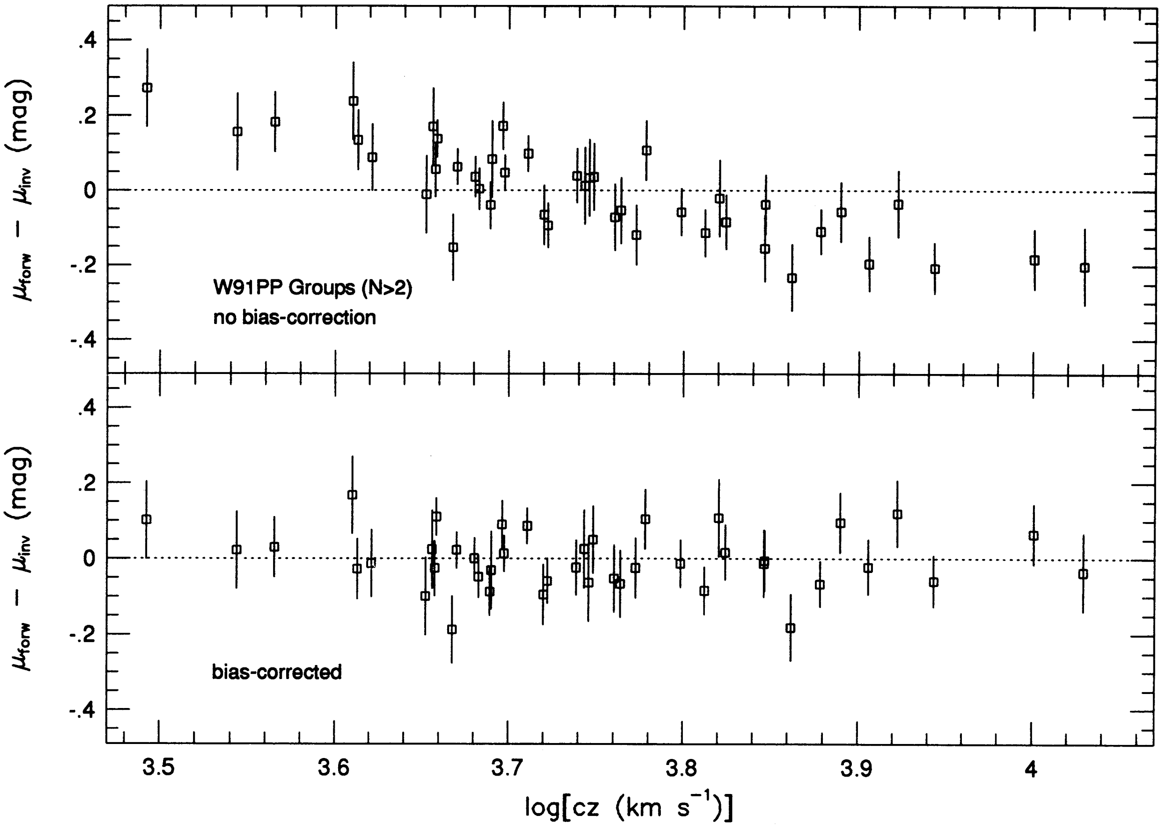

FIG. 13.—As Fig. 7, but for W91PP groups with three or more members

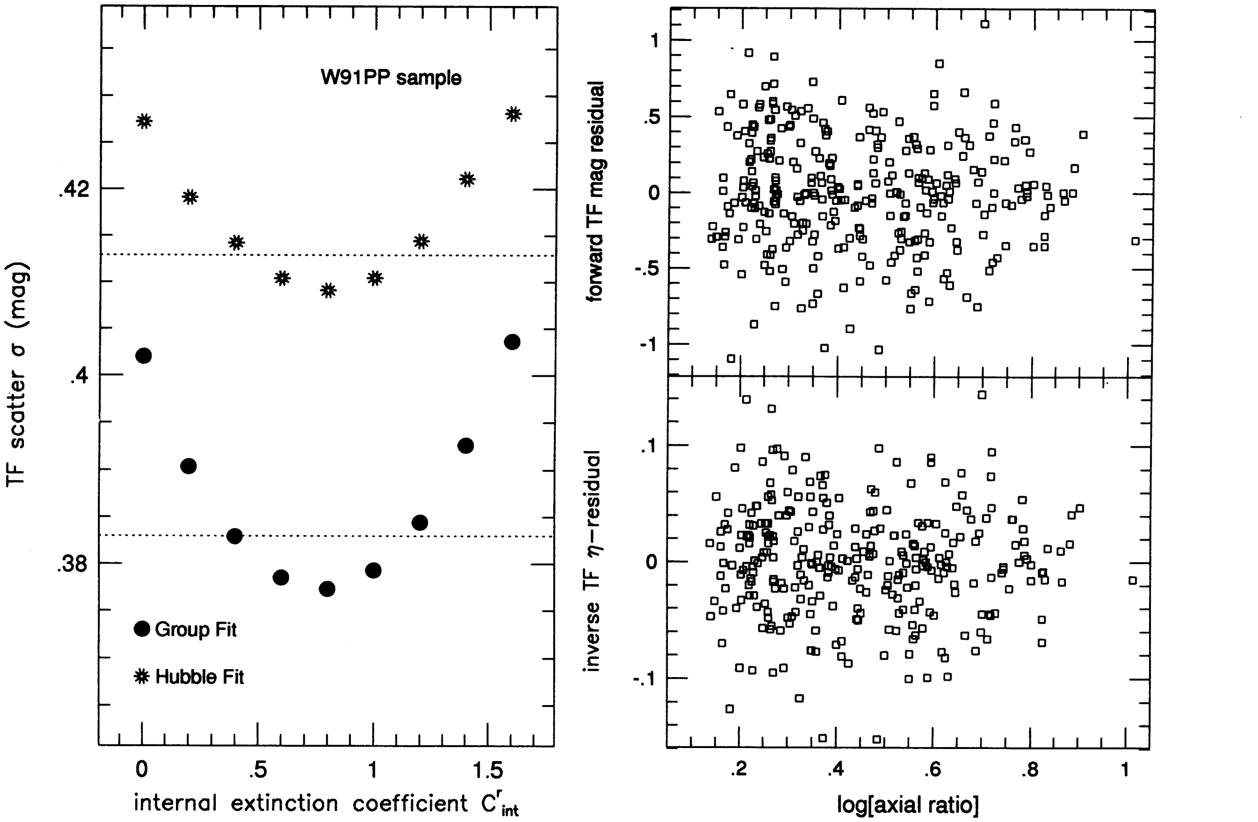

FIG. 14.—*Left:* W91PP TF scatter plotted as a function of the r-band internal-extinction coefficient $C^r_{\rm int}$. Hubble flow and $\sigma_{\rm in} = 0.40$ mag group scatters are shown. The horizontal dotted lines define 65% confidence intervals for $C^r_{\rm int}$. *Right:* Forward (*top*) and inverse (*bottom*) group TF fit residuals plotted against axial ratio, with the final adopted value $C^r_{\rm int} = 0.95$.

MAT sample, the fact that the inverse fit residuals do not correlate with axial ratio confirms that our determination of $C^r_{\rm int}$ has not been influenced by the selection-bias correction procedure.

3.2.1. *A Luminosity Dependence of $C^r_{\rm int}$?*

We again examine the claim by Giovanelli (1995) that internal extinction is luminosity dependent, now using W91PP. Because Giovanelli used I-band data, the comparison (unlike that earlier, which involved MAT) is not direct. Still, there is no reason for the effect to be specific to the I band, so the test is warranted again here. In Figure 15 we plot forward TF residuals versus the product $\eta\mathscr{R}$ (*top*) and inverse TF residuals versus the product $(M-D)\mathscr{R}$ (*bottom*), again from the $\sigma_{\rm in} = 0.4$ mag run of the grouping algorithm. Carrying out a linear fit of the apparent magnitude residuals to $\eta\mathscr{R}$, we find a slope of -0.14 ± 0.37; a fit of the η-residuals to $(M-D)\mathscr{R}$ yields a slope of 0.001 ± 0.006. These results confirm the visual impression that there is no significant trend in either plot. (Recall from the discussion of § 2.3.1 that the expected values of these slopes are ~ 1.0 and ~ 0.02, respectively, if the r-band data obeyed the luminosity-dependent extinction law proposed by Giovanelli for I-band data.) Thus, the W91PP TF fit confirms the result found above with the MAT sample, namely, that internal extinction is independent of luminosity or, equivalently, of velocity width.

4. THE CF SAMPLE

The selection criteria and observational methods used to acquire the CF sample are described in detail by Courteau (1996). CF is a sparse but full northern-sky survey consisting of a total of 326 Sb–Sc galaxies; in the present analysis we exclude the five "Zwicky only" objects and use the remaining 321 galaxies, all of which are found in the UGC catalog. The photometry used the same telescope/filter combination, and was reduced to the same system, as the W91 photometry. The CF velocity widths were optically determined but have been converted to a system equivalent to that of W91 (see Courteau 1992). In principle, then, we expect CF to follow the same TF relation as W91. However, we found in § 3 that W91CL and W91PP were themselves described by somewhat different TF relations. We must thus allow for the possibility that the CF TF relation differs as well. In what follows, we will estimate the slope of the TF CF relation using Hubble flow fits and find that it is fully consistent with that of the W91CL, but not of the W91PP, TF relation. Based on this consistency, we will adopt the W91CL TF slope for CF, but later (§ 6) we will separately determine the CF zero point. We adopt without further analysis the internal-extinction coefficient $C^r_{\rm int} = 0.95$ found for W91CL and W91PP (see Paper I and § 3.2), both because the CF and W91 photometric bandpasses are perfectly equivalent, and because CF is unsuitable for extinction-coefficient determination as it lacks high-inclination galaxies (Courteau 1992). We show below that with this choice the TF residuals do not correlate with axial ratio, as required.

The selection criteria for CF differ from those of W91. W91CL was selected to the limits of the UGC *and* the Zwicky catalogs; W91PP was selected to the UGC limit only. By contrast, CF was selected to the diameter limit (1′) of the UGC

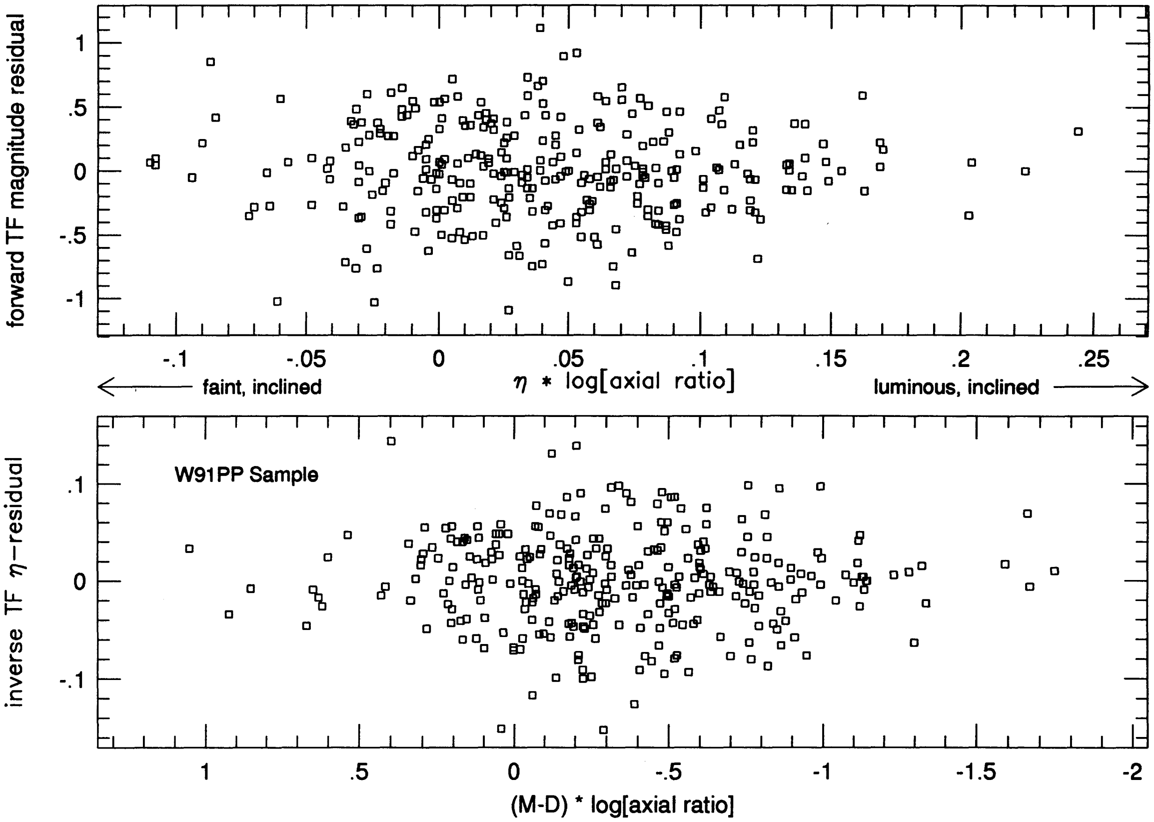

FIG. 15.—Forward (*top*) and inverse (*bottom*) TF residuals for the $\sigma_{\rm in} = 0.40$ mag W91PP groups plotted against the quantities that test for a luminosity dependence of internal extinction.

catalog, but with the additional requirement that the Zwicky magnitude be ≤ 15.5 mag. The CF sample is thus an example of the "two-criteria 'both-and'" selection procedure described by W94. We invoke the corresponding bias-correction formulae (see § 4.2.2 of W94) in the TF calibration for CF described below. We assume that the log $D_{\rm UGC}$-(m_r, η) and m_z-(m_r, η) are the same for CF as for W91CL and W91PP.

4.1. *Hubble Flow Fits*

The CF sample is too dilute for worthwhile application of the grouping algorithm. Thus, we use Hubble flow fits alone in studying its TF characteristics. We carry out these fits for both the entire CF sample and also for a "quiet Hubble flow" (QHF) subsample identified in the analysis of Courteau (1992) and Courteau et al. (1993). The QHF region is defined by the CF sample-selection geometry, plus the criteria $b > 0$, $cz > 3000$ km s^{-1} (the latter criterion ensures that objects are beyond the perturbative range of the Local supercluster), and includes 136 galaxies. Table 7 shows the results of the Hubble flow fits. The whole-sky fits are also restricted to $cz \geq 3000$ km s^{-1} in order to simplify comparison with the QHF fits. We have, as before, performed the fits in the LG, CMB, and heliocentric reference frames.

The TF slopes for the various QHF fits are all mutually consistent, with a typical value of $b \approx 8.05 \pm 0.30$. By comparison, the W91CL TF slope (Paper I) was $\sim 7.7 \pm 0.2$ while the W91PP TF slope (§ 3) was $\sim 7.1 \pm 0.2$. Thus, the CF TF slope is nominally larger than, but statistically consistent with, the W91CL TF slope. However, the CF slope differs significantly from the W91PP TF slope. It is worth noting that the TF slope consistency of the predominantly *field* CF sample with the *cluster* W91CL sample—as opposed to its inconsistency with the *field* W91PP sample—argues against the hypothesis that the slope differences are due to physical differences between field and cluster galaxies. In the left panel of Figure 16, we plot the TF relation resulting from the CMB Hubble flow fit for the QHF subsample. The absolute magnitudes on the vertical axis are computed as bias-corrected apparent magnitudes minus the "Hubble flow distance modulus" 5 log *cz*. Superposed on the points are the fitted CF TF relation, given in the second line of Table 7 (*solid line*), and the provisional W91CL TF relation (*dotted line*), given in Paper I. It is visually apparent

TABLE 7

CF TF RELATION FROM HUBBLE FLOW FITS

Reference Frame	A	$b\,(\pm)$	σ (mag)	N_σ
		QHF Region		
Heliocentric.......	−4.034	8.076 (0.312)	0.344	136
CMB	−4.102	8.010 (0.314)	0.348	136
Local Group......	−4.029	8.103 (0.319)	0.352	136
		All $cz \geq 3000$ km s^{-1}		
Heliocentric.......	−3.935	8.255 (0.260)	0.411	256
CMB	−3.863	8.478 (0.270)	0.426	256
Local Group......	−3.989	8.195 (0.263)	0.416	256

NOTE.—Parameters that result from fitting a foward TF relation to the CF sample, under the assumption of uniform Hubble flow in various frames.

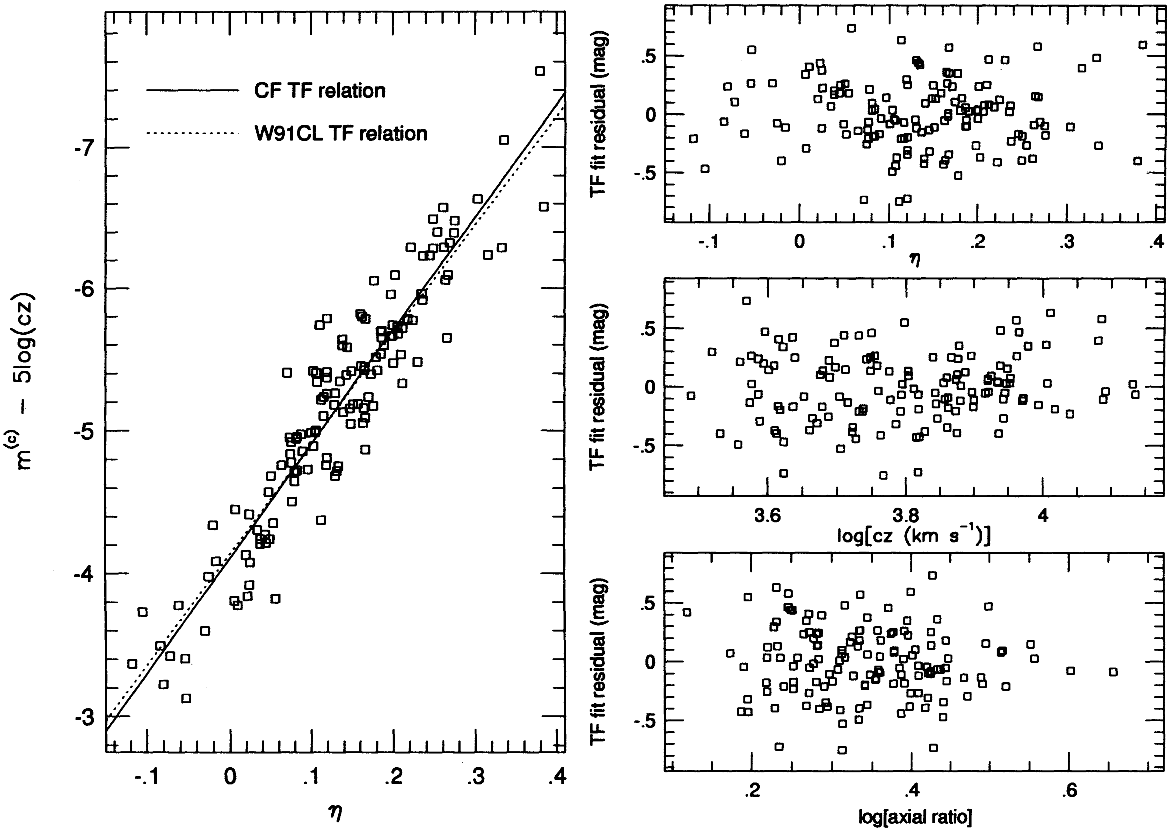

FIG. 16.—*Left:* CF TF relation obtained from a CMB-frame Hubble flow fit to the "quiet Hubble flow" subsample. The solid line represents the fitted TF relation while the dotted line is the provisional W91CL TF relation derived in Paper I. *Right:* Fit residuals with respect to η (*top*), log redshift (*middle*), and log axial ratio (*bottom*).

that the provisional W91CL TF relation is an acceptable fit to the CF QHF data. We therefore adopt it as the provisional TF relation for the CF sample as well. Since CF was designed for TF consistency with W91 (Courteau 1992), it is unsurprising but gratifying that we have confirmed this consistency here.[11]

In the right panels of Figure 16 we plot TF residuals from the QHF CMB Hubble flow fit. The top right panel shows no systematic trend of residuals with velocity width, which again confirms that a linear TF relation adequately describes the data. In the middle right panel, residuals are plotted against log redshift; no significant trend is seen, showing that the QHF velocity field is well modeled by uniform Hubble flow, as assumed. In the bottom right panel, TF residuals are plotted as a function of log axial ratio. Again, there is no visible trend. This shows that, although we have simply adopted the value $C^r_{\rm int} = 0.95$ obtained from the W91CL and W91PP analyses, this value adequately describes the CF data as well, as expected.

Restricting our attention to the QHF fits, we find a best TF scatter $\sigma \approx 0.34$–0.35 mag. (This agrees well with the result obtained, using a somewhat different technique, by Courteau 1992.) However, when the entire sample is considered, the scatter is $\sigma \gtrsim 0.41$ mag, comparable to the W91PP Hubble flow fit scatter. One interpretation is that in the QHF region we see the true TF scatter, while in the overall sample the scatter is inflated by peculiar velocities. While the second part of this interpretation is probably true, the first is not necessarily so. Our freedom of choice in delineating this region in effect constitutes additional free parameters in the fit. Moreover, the rms statistical uncertainty in the scatter estimate from 136 galaxies (134 degrees of freedom) is ~ 0.02 mag. We adopt here the conservative approach of assigning the same TF scatter, 0.38 mag, to the CF sample as we have to the larger and statistically better constrained W91PP sample.

As with other samples, the CMB fits do not minimize TF scatter; for both the QHF and full-sky $cz \geq 3000$ km s^{-1} subsamples, the heliocentric fits yield a scatter smaller than or comparable to the CMB fits. This most likely arises, as we have suggested before, from the existence of large-scale bulk flows with respect to the CMB frame.

5. THE A82 SAMPLE

The A82 sample is based on the nearby ($cz \lesssim 3000$ km s^{-1}) H-band sample of Aaronson et al. (1982). The A82 photometry has recently been modified by Tormen & Burstein (1995, hereafter TB95), who also made slight changes in the sample makeup. TB95 redetermined accurate blue diameters and used them to produce new H-band magnitudes $H_{-0.5}$. Adopting an H-band Galactic extinction correction of $0.1 A_B$, TB95 presented corrected magnitudes $H^g_{-0.5}$, which we use here. In addition, we apply the redshift correction derived by Aaronson et al. (1980) for the H-band, as we will discuss further in Paper III.

---

[11] In § 6, we will find a marginally significant difference between the CF and W91CL final TF zero points. We remain without a fully satisfactory answer as to why W91PP differs from W91CL and CF in terms of TF slope. The most likely explanation, as mentioned above, is that velocity-width inconsistencies are responsible.

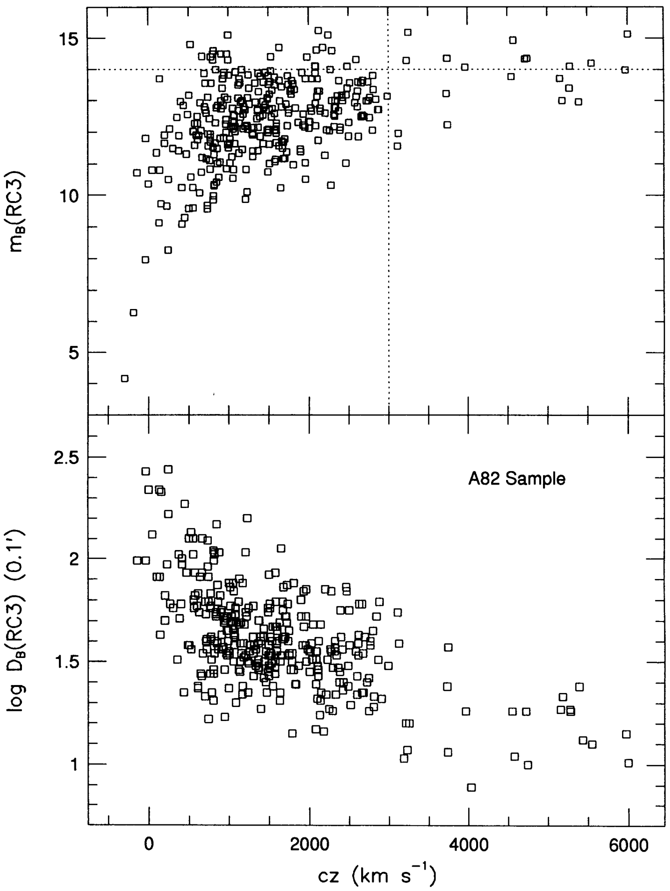

FIG. 17.—Selection criteria for the A82 sample. The upper panel shows the RC3 catalog *B*-band raw magnitude plotted against redshift. The dotted lines indicate the cuts made in *B* magnitude and redshift to generate an approximately complete sample. The bottom panel shows RC3 catalog *B*-band diameters plotted against redshift; a cut on diameter would not produce a good approximation to a complete sample.

The internal-extinction correction is discussed below in connection with the TF calibration. We have retained the raw velocity widths of Aaronson et al. (1982) but have recomputed inclinations, and thus deprojected widths, using axial ratios derived from the RC3 catalog (see TB95).

The total sample listed by TB95 consists of 359 objects. However, we make two important cuts, one on redshift and one on *B*-band apparent magnitude, to improve completeness. In Figure 17, we plot the RC3 raw apparent magnitude (*top*) and diameter (*bottom*) versus heliocentric redshift. The figure shows that the sample is neither magnitude nor diameter limited in a strict sense. However, in the upper panel the points congregate near an upper limit of m_B(RC3) ≈ 14.0 mag for all $cz \lesssim 3000$ km s^{-1}. This suggests that if we eliminate the relatively few fainter objects, the remaining objects will constitute an approximately magnitude-limited sample. The diameter plot does not exhibit the same degree of clustering toward a limit, indicating that a cut on diameter will not produce a sample with well-defined selection criteria. For $cz > 3000$ km s^{-1}, a higher proportion of galaxies are faint in m_B(RC3), and the density of objects is greatly reduced. We thus restrict the sample to heliocentric redshifts less than 3000 km s^{-1} and to m_B(RC3) ≤ 14.0 mag. These limits are shown as dotted lines in Figure 17. The result is a restricted A82 sample with selection criteria that are sufficiently well defined for application of the W94 bias-correction procedure. It is this 300 galaxy sample that forms the basis of the TF calibration analysis presented here.

5.1. *Selection Criteria Relations for A82*

As with other samples, we fit the selection quantity, in this case m_B(RC3), to the TF observables in order to quantify sample selection for the W94 bias-correction procedure. We depart here slightly from our earlier approach in that we use the Galactic extinction–corrected *H*-band magnitudes, which we refer to as m_H in keeping with our earlier notation, in this fit. We assume that m_B(RC3) is related to the TF observables by an expression analogous to equation (14) of Paper I. In carrying out the fit, we use only galaxies with m_B(RC3) ≤ 14.0 mag, and bias-correct accordingly. The results of the fit are presented in Table 8.

In the left panel of Figure 18, we plot the m_B(RC3)-m_H relation; the RC3 *B* magnitudes have been corrected for bias and thus can exceed their maximum raw value of 14.0 mag. However, relatively few objects have bias-corrected *B* magnitudes fainter than the limit. This guarantees that the bias corrections in the TF calibration analysis will be relatively small. The right panels show residuals from the fit with respect to η and redshift. The upper right panel shows that there is no trend with η (as is to be expected, since it was a fitted variable). This verifies the rather significant η-coefficient of 2.915 seen in Table 8, which is due to a velocity-width dependence of the *B*-*H* color. The lower right panel shows that there is no residual redshift dependence, although *cz* was not a fitted variable. If we were to fit *cz* rather than η, we could also eliminate both η- and *cz*-dependences in the fit. However, the fit that involves η and not *cz* produces smaller scatter, and we assume this fit is the better one. This assumption has little effect on our treatment of selection biases.

5.2. *Calibration of the A82 TF Relation*

We proceed as we did with MAT and W91PP, i.e., we first carry out Hubble flow fits, and then apply the grouping algorithm.

TABLE 8

FIT COEFFICIENTS FOR A82

QUANTITY PREDICTED	CONSTANT	COEFFICIENT OF m_H	η	A_B	$\mathscr{R}$	log cz − 3.7	σ (mag)
m_B(RC3)......	2.697	0.919	2.915	0.885	1.449	0.000	0.372

NOTES.—Coefficients of the indicated quantities in the linear relation for m_B, the RC3 (raw) blue magnitude, for the A82 sample. Also given is the rms dispersion for this relation. The RC3 *B*-magnitude limit for the fit was 14.0 mag.

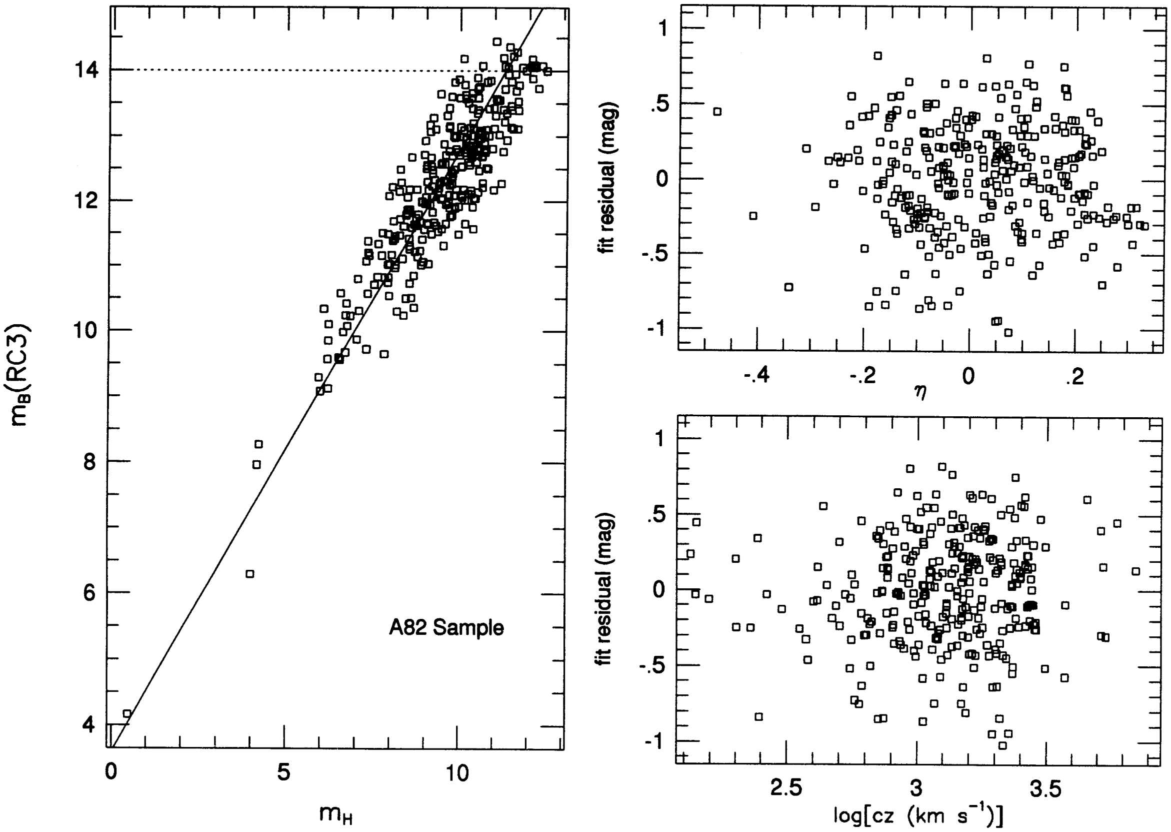

FIG. 18.—*Left:* Bias-corrected RC3 catalog magnitudes plotted against H-band (Galactic extinction corrected) magnitudes for the A82 sample. The dotted line shows the B-band diameter limit; the bias-corrected magnitudes can be fainter than this limit. *Right:* Residuals from the m_B-m_H fit plotted against η (*top*) and log redshift (*bottom*).

5.2.1. *Preliminary Hubble Flow Fits*

The results of Hubble flow fits in three frames are shown in Table 9. Because many of the A82 galaxies are very nearby, where even slight departures from Hubble flow lead to large TF residuals, we have restricted the fits to objects with heliocentric redshifts ≥ 750 km s^{-1}. The scatters resulting from these fits are greatly in excess of those obtained from the CCD samples. However, as the grouping-algorithm results will show, most of this increased scatter is due to the inadequacy of the Hubble flow model for the nearby A82 sample. Despite the large scatter, the slopes and zero points of these fits provide a satisfactory preliminary TF relation for the A82 sample. In this case we adopt the CMB fit, which has the smallest scatter, for this purpose.

TABLE 9

A82 TF RELATION FROM HUBBLE FLOW FITS

Reference Frame	A	b	σ (mag)	N_σ
Heliocentric.......	−5.698	10.513	0.642	248
CMB	−5.813	10.418	0.620	248
Local Group......	−5.658	10.670	0.640	248

NOTES.—Parameters that result from fitting a forward TF relation to the A82 sample, under the assumption of uniform Hubble flow in heliocentric, CMB, and LG frames of reference. N_σ is the number of objects (those with fit residuals less than 2.0 mag) used in the scatter computation. In all cases objects participating in the fit were required to satisfy $cz \geq 750$ km s^{-1} (heliocentric).

5.2.2. *Application of the Grouping Algorithm to A82*

A problem with grouping A82 is that, while the algorithm assumes a "cold" velocity field (§ 2.2.2), A82 includes the Virgo region, in which large virial motions are present. To account for this, we have set the radial velocities of 22 galaxies equal to that of the Virgo Cluster. These objects were chosen for highly probable Virgo Cluster membership; they will be identified in Paper III.

As before, we use the Kolatt (1995) simulation of the A82 sample to help us interpret the results of the A82 grouping. We apply the grouping algorithm to both the simulated and real A82 samples for a range of input scatters. Figures 19 and 20 show the behavior of the output scatter $\sigma_{\rm out}$, and of other diagnostic quantities, as a function of $\sigma_{\rm in}$ for the simulation and real data, respectively. Both plots show the characteristic $\sigma_{\rm out}$ versus $\sigma_{\rm in}$ behavior seen for other samples. The $\sigma_{\rm out}$-$\sigma_{\rm in}$ plot in Figure 19 does not constrain the proper value of $\sigma_{\rm in}$ as tightly as it did for the earlier samples. This results from the much poorer statistics of the simulated A82 sample, in which only ~ 150 objects were assigned to typically rather small groups. Still, the behavior is consistent with what was seen earlier, and it is reasonable to assume that the rule of thumb ($0.95 \lesssim \sigma_{\rm in}/\sigma_{\rm out} \lesssim 1.25$) obtained with MAT and W91PP is roughly valid here. The correspondence of this regime of the $\sigma_{\rm out}$-$\sigma_{\rm in}$ diagram with the onset of the plateau in the percentage of objects grouped lends credence to this assumption. Application of this rule to the real data shows that $\sigma_{\rm out}$ is a valid estimate of the true A82 TF scatter for the runs with 0.45 mag $\lesssim \sigma_{\rm in} \lesssim 0.6$ mag. This leads to the estimate

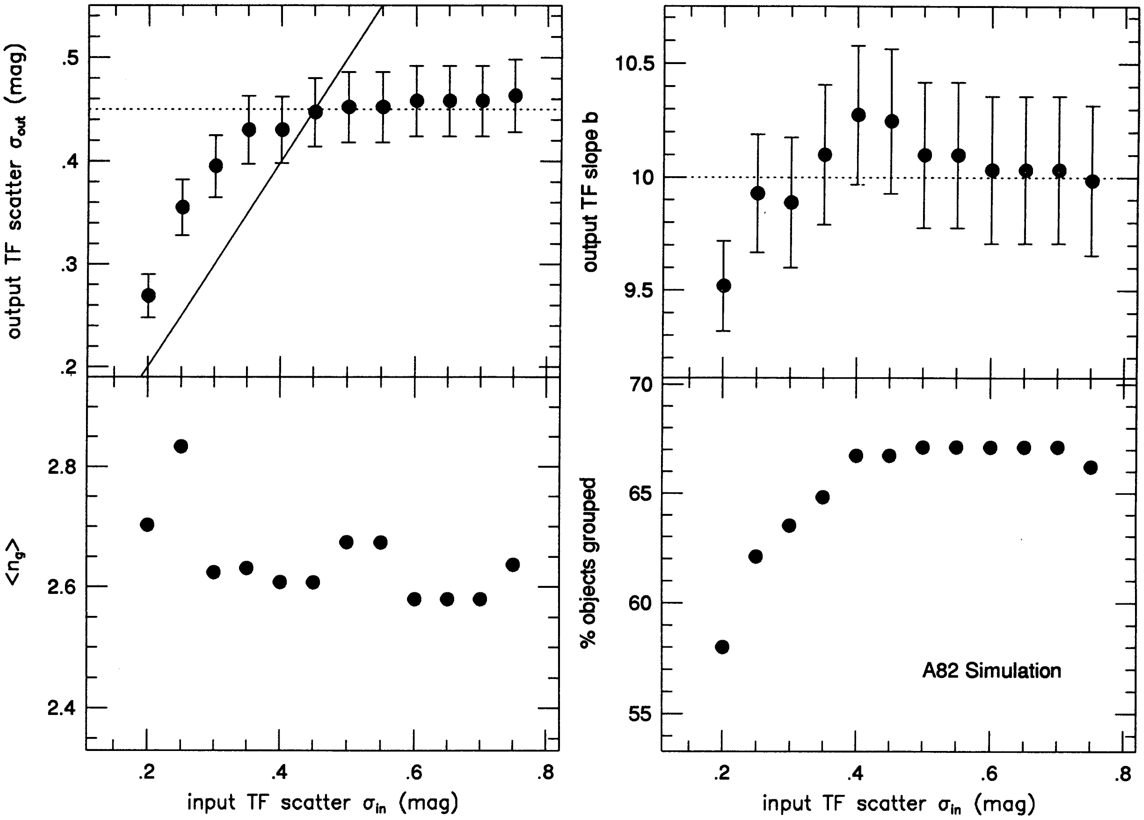

FIG. 19.—Same as Fig. 4, but results for the simulated A82 sample are shown

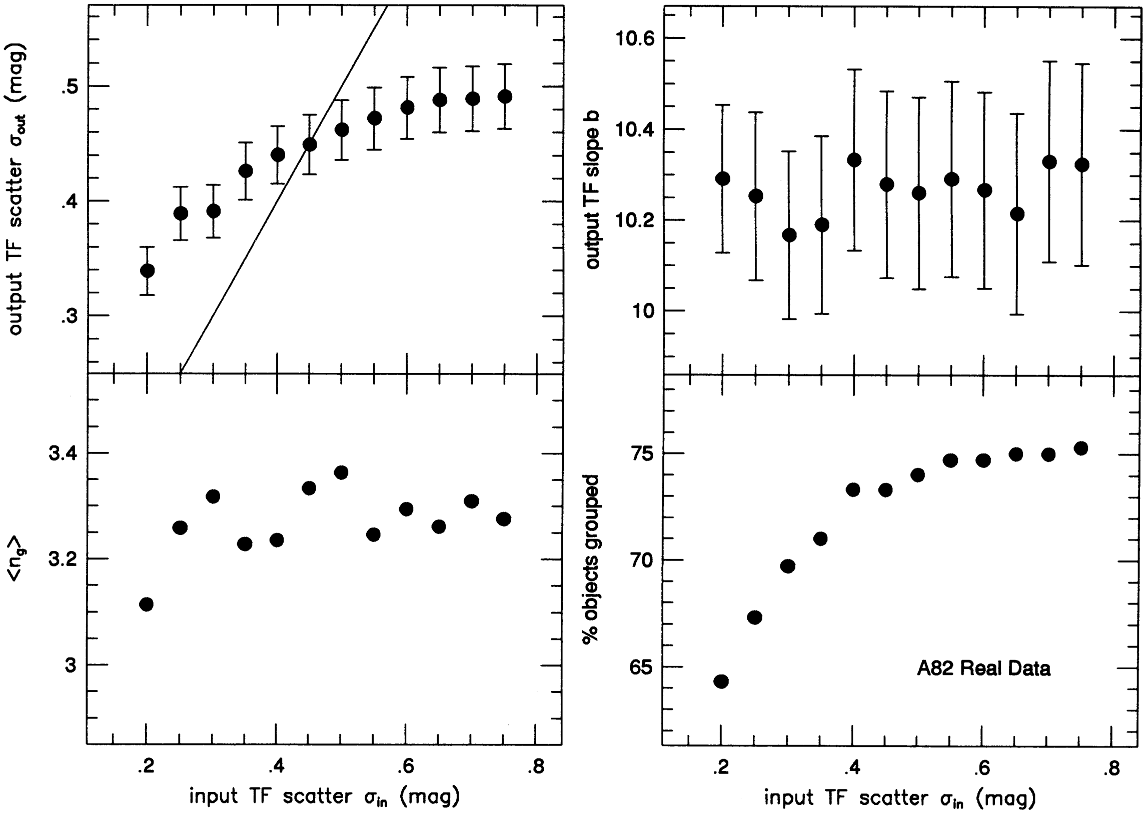

FIG. 20.—Same as Fig. 4, but results for the real A82 sample are shown

TABLE 10

PARAMETERS OF THE PROVISIONAL A82 TF RELATIONS

	FORWARD			INVERSE		
SAMPLE	A	b (±)	σ (mag)	D	e (±)	σ_η
A82......	−5.81	10.29 (0.22)	0.47	−5.85	0.0893 (0.0018)	0.043

NOTES.—Parameters of the provisional A82 forward and inverse TF relations. The slopes and scatters, which are final, were obtained from the $\sigma_{\rm in}$ = 0.55 mag run of the grouping algorithm. The zero points remain to be adjusted through an overlap comparison with other samples.

$\sigma = 0.465 \pm 0.015$ mag. However, as was the case with W91PP, this systematic uncertainty is smaller than the statistical uncertainty of 0.027 mag, and the latter is therefore a more realistic measure of the rms scatter uncertainty for A82. As in previous cases, the output scatter asymptotes to a limiting value ($\sim$0.49 mag) as $\sigma_{\rm in}$ is made very large.

5.2.3. *The Provisional A82 TF Relation*

We adopt the slope and scatter from the $\sigma_{\rm in}$ = 0.55 mag run of the grouping algorithm. Combining these with the CMB Hubble flow fit TF zero point, we obtain the provisional A82 TF relation presented in the three columns of Table 10 labeled "Forward." In the left panel of Figure 21, we plot the H-band TF relation from the $\sigma_{\rm in}$ = 0.55 mag groups. In the right panels of the figure we plot TF residuals with respect to η and A_B. The assumption of a linear TF relation is seen to be a good one. There is no strong evidence of a decrease in scatter with increasing velocity width. There is no trend of residuals with A_B, which validates our adopted Galactic extinction corrections for A82.

5.2.4. *Physical Significance of the Hubble Flow versus Group TF Scatter*

In contrast with MAT and W91PP, the A82 group TF scatter is considerably smaller than the scatter obtained from the Hubble flow fits—even when $\sigma_{\rm in}$ is made arbitrarily large. This is clear evidence that the inflated scatter in the Hubble flow fits results from real peculiar velocities. The very significant reduction in scatter as compared with the Hubble flow fits does not reflect larger peculiar velocities in the A82 sample as compared with MAT or W91PP but instead the much smaller mean distance, $\sim$1500 km s^{-1}, of A82-sample galaxies. Specifically, the amplitude of the mean radial peculiar velocities indicated by the scatter difference is $\sim(\ln 10/5)(0.62^2 - 0.47^2)^{1/2} 1500$ km s$^{-1} \approx 280$ km s^{-1}, comparable to the values obtained with MAT and W91PP.

5.2.5. *An Inverse TF Relation for A82*

We fit an inverse TF relation to the A82 groups formed by the preferred $\sigma_{\rm in}$ = 0.55 mag run of the grouping algorithm. The inverse slope e and scatter σ_η resulting from this fit are given in Table 10. Also given is a provisional TF zero point D, obtained from a CMB Hubble flow inverse TF fit. In the inverse fits, we corrected for the selection bias due to the η-dependence of the sample-selection criteria indicated in Table 8.

5.2.6. *Validating the Bias Corrections*

In Figure 22, we plot forward-minus-inverse TF distance moduli for the A82 groups. In the upper panel the forward

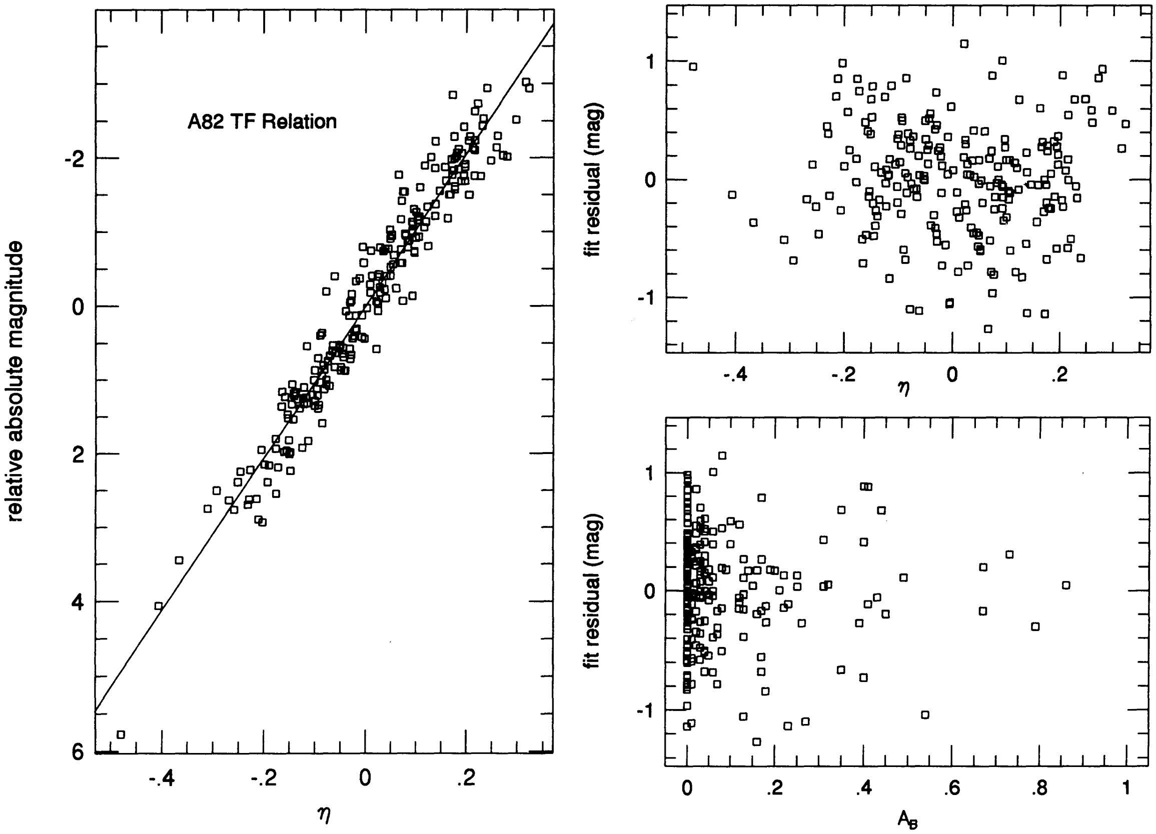

FIG. 21.—*Left:* A82 TF relation fitted to the $\sigma_{\rm in}$ = 0.55 mag groups. The solid line plotted through the points shows the fitted slope of 10.29. *Right:* TF residuals from this fit with respect to η (*top*) and Galactic extinction (*bottom*).

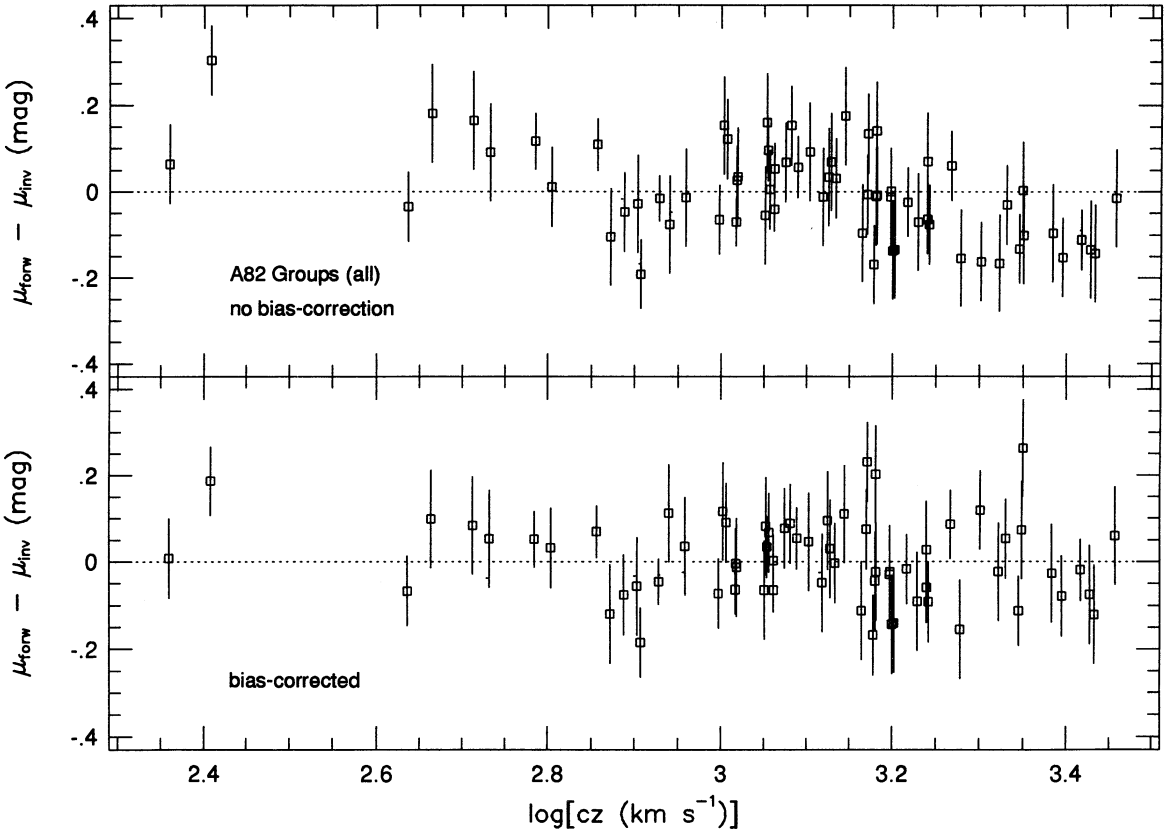

FIG. 22.—As Fig. 7, but for all A82 groups

moduli have not been corrected for selection bias, while in the lower panel they are bias-corrected. We plot groups of all sizes since most of the more distant ($cz \gtrsim 2000$ km s^{-1}) A82 groups contain only two members. The uncorrected modulus differences exhibit the characteristic trend seen in earlier cases: the forward TF fit underestimates the distances of higher redshift groups. The trend is somewhat milder than in earlier instances because (as already noted) the level of bias in the A82 sample is smaller because most sample objects are quite local. A linear fit of [μ(forw) − μ(inv)] for the uncorrected moduli to log cz yields a slope of -0.235 ± 0.049, a significant trend, though less so than for MAT and W91PP. When the same fit is carried out for the corrected moduli, the resulting slope is -0.066 ± 0.049, indicating that the bias-correction procedure has successfully eliminated any significant trend.

5.2.7. *Determination of the A82 Internal-Extinction Coefficient*

The nature of H-band internal extinction differs from that which affects the CCD magnitudes. The H-band photometry derives from aperture magnitudes scaled to a diameter-dependent "standard" aperture (see, e.g., TB95). Thus, inclination effects on the diameters and magnitudes are entangled. There is indeed no a priori reason that $C^H_{\rm int}$ must be positive—and in fact, we have used $C^H_{\rm int} = -0.3$ in the analysis of the previous section. We arrived at this value through our usual approach, by assuming that the proper value of $C^H_{\rm int}$ for our purposes is obtained by minimizing TF residuals.

We apply the test to both the CMB Hubble flow fit and the $\sigma_{\rm in} = 0.55$ mag groups. The results are shown in the left panel of Figure 23. The group TF scatter (*bottom*) minimizes for $C^H_{\rm int} \approx -0.25$ while the Hubble flow scatter minimizes for $C^H_{\rm int} \approx -0.35$. The negative signs imply that we must correct the H-band magnitudes *faintward* in order to minimize TF scatter, i.e., that the observed magnitudes become *brighter* with increasing inclination. This is the opposite of the usual effect and (if the effect is real) is presumably due to small increases in diameter with inclination. The effect is not detected with high significance: as can be seen from the 65% confidence intervals indicated as dotted lines on the plot, the null value $C^H_{\rm int} = 0$ is only marginally ruled out from the Hubble flow fit and is within the 65% confidence interval for the group fit. Nonetheless, our practice has been to adopt the values of $C_{\rm int}$ that minimize TF scatter, and we continue to do so here despite the weak detection. We adopted the average of the Hubble flow and group minima, $C^H_{\rm int} = -0.30$, as our final value. The right panels of Figure 23 show forward (*top*) and inverse (*bottom*) TF residuals for the $\sigma_{\rm in} = 0.55$ mag group fits. The residuals do not correlate with axial ratio in either case, confirming our adopted value of $C^H_{\rm int}$ and demonstrating its independence from the bias-correction procedure.

6. PLACING THE SAMPLES ON A COMMON ZERO POINT

Of the various samples discussed here and in Paper I, we have computed a final TF zero point only for the HM cluster sample. We have obtained provisional TF zero points for the other samples using the assumption that redshift equals distance, as we did for HM. But we cannot rely on this assumption for these other samples, as they lack either the wide sky coverage (W91CL, W91PP, CF, MAT) or the depth (A82) of HM. We must therefore obtain final zero points for these

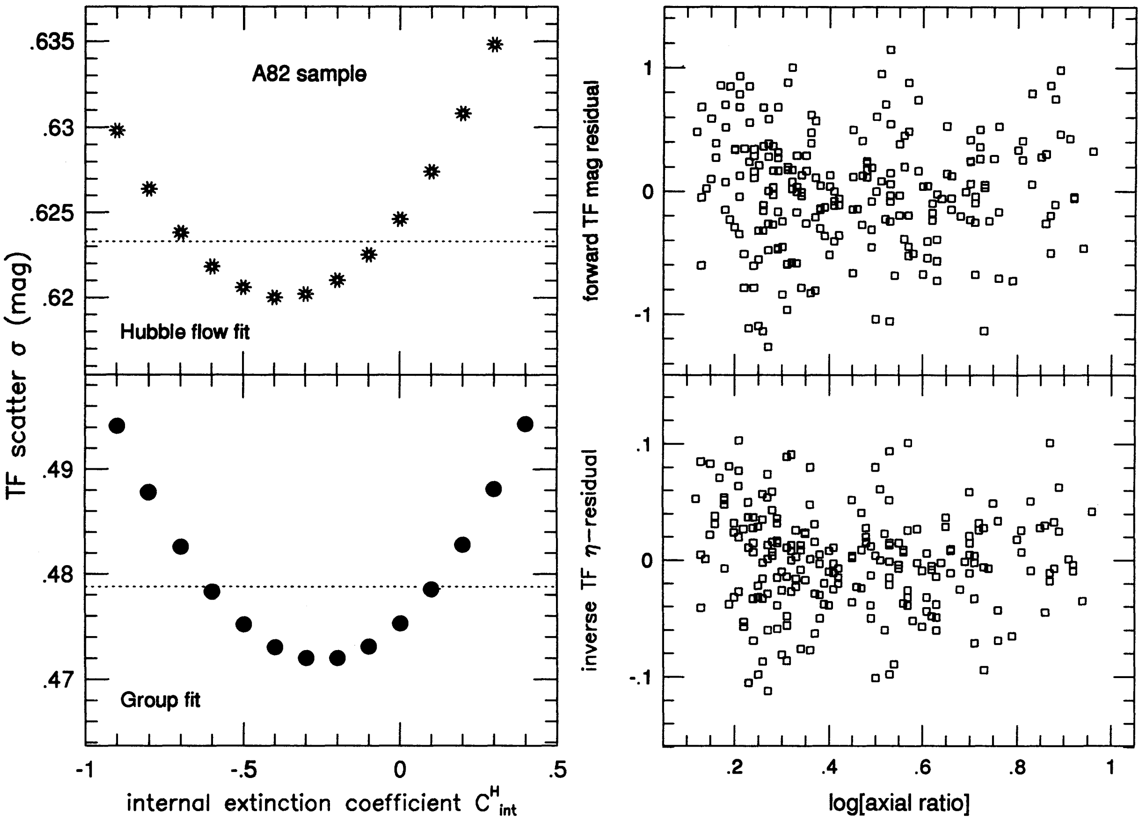

FIG. 23.—*Left:* A82 TF scatter plotted as a function of the H-band internal extinction coefficient $C^H_{\rm int}$. Hubble flow (*top*) and group scatters (*bottom*) are shown. The horizontal dotted lines define 65% confidence intervals for $C^H_{\rm int}$. *Right:* Forward (*top*) and inverse (*bottom*) group TF fit residuals plotted against axial ratio, with the final adopted value $C^H_{\rm int} = -0.30$.

samples by comparison with HM. In this section, we do so by comparing data for objects common to two or more of the individual samples ("overlap" objects).

The basic idea is simple. For each galaxy common to two samples, we compute the TF distance moduli, $\mu_1 = m_1 - (A_1 - b_1\eta_1)$ and $\mu_2 = m_2 - (A_2 - b_2\eta_2)$, assigned that galaxy by samples 1 and 2, respectively. Suppose that sample 2 has already been assigned a final TF zero point. We then adjust the provisional TF zero point A_1 so the difference $\Delta\mu = \mu_2 - \mu_1$ vanishes when suitably averaged over all objects common to samples 1 and 2. For this average we in fact use one-half the sum of the median plus the mean modulus difference, rather than a straight mean, in order to enhance robustness. The final zero point for sample 1 is then just the provisional zero point minus the "average" distance-modulus difference in the sense just described.

The discussion of the previous paragraph refers to the forward TF relation. For the inverse TF relation, we carry out a perfectly analogous procedure, except that now the individual object distance moduli are computed as $\mu = m - (D - e^{-1}\eta)$.

We carry out this overlap procedure hierarchically, i.e., we zero-point each sample relative to all those already zero-pointed. This requires that we order the samples for the overlap comparison. We have done so as follows: First, we overlap-compare W91CL with HM and adjust the zero point of W91CL accordingly. Then we overlap-compare W91PP with W91CL and HM and adjust its zero point. We then compare CF with the previous three, MAT with the previous four, and finally A82 with the previous five. (As it turns out, A82 has no overlap with W91PP; moreover, we neglect the objects in common between A82 and W91CL, for reasons discussed below.) It should be pointed out that the final zero points depend slightly on the order chosen for performing the overlap. However, this dependence is small, and the order we have chosen maximizes the number of comparison objects at each step.

In Table 11, we summarize the results of the overlap comparisons. Column (1) gives the name of the sample whose zero point is to be adjusted, while column (2) gives the name of the already zero-pointed sample(s) with which the comparison is made. Columns (3) and (4) give the average distance-modulus differences, in the sense of "sample 2 minus sample 1," for the forward and inverse TF relations, respectively. The quantity in parentheses that follows the forward modulus difference is the 1 σ statistical uncertainty in that quantity; the corresponding error in the inverse modulus difference differs negligibly from the forward. Column (5) gives the rms scatter about the average (from the forward TF relations; again, the inverse yields essentially the same scatter), and column (6) the total number of overlap objects involved in the comparison. The lines of the table in which column (2) consists of all previously zero-pointed samples list the values of $\Delta\mu$ ultimately adopted for the zero-point adjustment. Note that the value of $\Delta\mu$ in those lines is not necessarily a weighted average of the values in the preceding lines; this is because we have used one-half median plus mean, rather than straight means, in computing $\Delta\mu$.

TABLE 11

OVERLAP COMPARISON OF TF SAMPLES

SAMPLE 1 (1)	SAMPLE 2 (2)	$\Delta\mu[2-1]$ (mag) Forward (3)	$\Delta\mu[2-1]$ (mag) Inverse (4)	σ_μ (mag) (5)	N_μ (6)
W91CL	HM	0.043 (0.019)	0.092	0.202	114
W91PP	HM	−0.001 (0.025)	0.001	0.176	49
W91PP	W91CL	−0.008 (0.030)	−0.015	0.150	26
W91PP	HM + W91CL	−0.004 (0.019)	−0.005	0.166	75
CF	HM	0.151 (0.043)	0.208	0.297	47
CF	W91CL	0.093 (0.030)	0.142	0.175	35
CF	W91PP	0.042 (0.036)	0.110	0.254	49
CF	HM + W91CL + W91PP	0.083 (0.022)	0.154	0.249	131
MAT	HM	−0.086 (0.039)	−0.144	0.336	74
MAT	W91CL	−0.086 (0.064)	−0.163	0.213	11
MAT	W91PP	0.051 (0.060)	−0.004	0.255	18
MAT	CF	0.037 (0.060)	−0.010	0.210	12
MAT	HM + W91CL + W91PP + CF	−0.044 (0.029)	−0.110	0.310	115
A82	HM	0.128 (0.088)	0.184	0.411	22
A82	CF	0.091 (0.086)	0.131	0.485	30
A82	MAT	0.148 (0.049)	0.203	0.438	80
A82	HM + CF + MAT	0.139 (0.038)	0.183	0.441	132

NOTES.—Results of intercomparing the TF distance moduli of galaxies common to two or more individual samples. For each sample, the comparison is done with all previously zero-pointed samples. The quantities σ_μ and N_μ are, respectively, the rms scatter of the distance-modulus comparison and the number of objects used in the calculation. The overlap comparison is not necessarily limited to those objects that constitute the "complete samples" used in the TF calibrations.

We have not included 20 galaxies in common between A82 and W91CL in the A82 overlap comparison. These galaxies are exclusively in the Ursa Major Cluster. Their average $\Delta\mu$ was smaller, by ~0.15 mag, than the value shown in the "A82 versus others" line. The A82 versus W91CL comparison also had very small scatter (~0.20 mag), so the discrepancy is quite significant. The source of the discrepancy lies in the velocity widths used for the Ursa Major galaxies in W91CL. These widths came from the compilation of Aaronson et al. (1982) and are not statistically equivalent to the 20% velocity widths used in the remainder of the W91CL sample, as we will show in Paper III. Since the Ursa Major galaxies do not figure anywhere else in Table 11, this velocity-width difference plays no role in any of the other overlap comparisons. If we were to include the 20 Ursa Major galaxies, the final zero-point shift for A82 would change by only 0.04 mag, which is comparable to the statistical error in any case.

In Figure 24, we plot the individual object forward TF distance modulus differences, following the final zero-point adjustments, as a function of log redshift. The plots show that there are no significant trends with redshift for any of the samples. The differences in the scatters of the overlap comparisons for the various samples, listed in Table 11, are visually apparent in the plot. From top to bottom there is a progression toward larger scatter; note in particular that the A82 panel has an expanded vertical scale.[12] These differing scatters reflect the greater or lesser degree of correlation of measurement errors, as we discuss further in § 7.2.

7. ON THE VALUE OF THE TF SCATTER

Accurate estimation of the TF scatter σ is vitally important, as σ determines both the random errors in velocity analyses and systematic errors due to Malmquist and selection biases. It is the overall or "observed" scatter that plays this role, not the individual contributions (intrinsic scatter and measurement error) to it. In this section, we first discuss the observed scatter obtained from our analysis and then estimate the intrinsic TF scatter using the results of the overlap comparison.

7.1. *The Observed TF Scatter*

Given the importance of the TF scatter, it is perhaps surprising that recent estimates have varied so widely. Many estimates based on CCD samples have found $\sigma \lesssim 0.3$ mag (e.g., Bothun & Mould 1987; Pierce & Tully 1988; Willick 1991; Mathewson et al. 1992; Schommer et al. 1993; Giovanelli et al. 1995). Bernstein et al. (1994) reported $\sigma = 0.1$ mag from an *I*-band study of galaxies in the Coma supercluster. By contrast, Sandage and coworkers (Sandage 1994; Federspiel et al. 1994) have found $\sigma \gtrsim 0.5$ mag using the MAT sample that we have analyzed here. Our own analysis points to a typical scatter of ~0.4 mag for CCD-based samples and a somewhat larger value of ~0.47 mag for the *H*-band A82 sample. What are the sources of these divergent estimates?

The least important (though by no means negligible) is the "dispersion bias" discussed by W94, an effect that has been largely ignored in previous work. The magnitude- and/or diameter-limited nature of most samples results in the apparent scatter being smaller than the true value. We have treated this effect using the W94 bias-correction procedure, with the corrected scatters typically ~5% larger than the uncorrected

---

[12] That plot also extends to redshifts beyond 3000 km s^{-1}; as explained in the notes to Table 11, the overlap comparisons are not limited to the "complete samples" used in TF calibration.

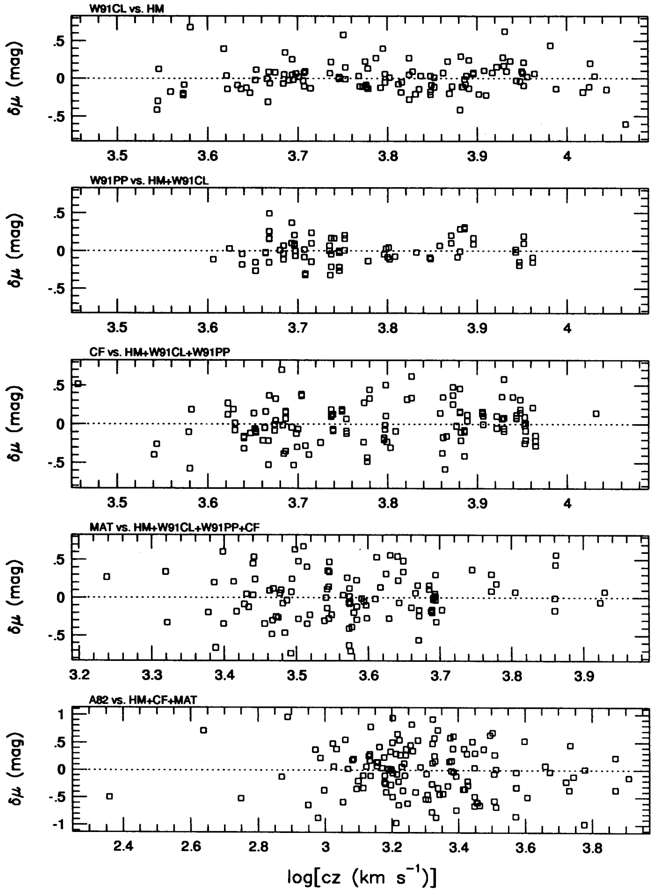

FIG. 24.—Individual object forward TF distance modulus differences, after final adjustment of the TF zero points by the overlap procedure. The various panels represent the five separate sample intercomparisons made in determining relative TF zero points. Note the expanded vertical scale of the bottom panel.

ones. The second most important factor is differing treatments of the effect of peculiar velocities on scatter computation. If we had operated on the assumption that peculiar velocities were negligible, we would have been obliged to adopt the scatter values stemming from our Hubble flow fits. In that case, our estimated scatter for the MAT and W91PP samples would have exceeded our final estimates (obtained from the grouping analysis) by ~10% while our estimate of the A82 scatter would have exceeded our final estimate by ~30%. Sandage and coworkers have generally assumed that peculiar velocities make a very small contribution to the TF scatter, and thus derive higher values than we do. We have not made specific a priori assumptions about the amplitude of peculiar motions in our analysis. However, we have allowed for their existence, using the grouping algorithm to disentangle their effects from actual TF scatter. The reduction of scatter in the group as compared with the Hubble flow TF calibrations led to a consistent value of ~250 km s^{-1} for the rms amplitude of radial peculiar motions, for three samples with very different spatial characteristics. While by no means proof, this consistency lends credence to our procedure.

The third and most important source of variant scatter estimates is the subjective element involved in excluding certain deviant objects from the scatter computation. The TF scatter is generally computed as an rms dispersion about a mean relation. This statistic can be very sensitive to outliers, especially in small samples. Some of the studies cited above, recognizing this sensitivity, liberally excluded objects judged to be "outliers." In studies that estimate the TF scatter using cluster samples (Bothun & Mould 1987; Pierce & Tully 1988; Willick 1991; Mathewson et al. 1992), one is free to argue that certain galaxies "are not cluster members" and thus exclude them. However, the decision to exclude may be influenced as much by the fact that an object has a large TF residual as on "objective" criteria. In their TF study of a subsample with extraordinarily small TF scatter, Bernstein et al. (1994) liberally purged objects deemed unacceptable, based on considerations of data quality and galaxy morphology. While these considerations appear "objective," the remaining 23 objects on which their scatter estimate is based are unrepresentative of the large, complete samples needed for peculiar velocity studies.

Our approach has been more conservative with regard to exclusion of objects than the studies, cited above, that have estimated small ($\lesssim 0.3$ mag) TF scatter. Unlike Bernstein et al., we have not required our sample objects to exhibit "clean" morphology or data of exceedingly high quality. We have, however, excluded a small fraction (~1%–2%) of all galaxies from scatter computations. In Paper I, several HM, and one W91CL, cluster galaxies were excluded because of excessively ($\gtrsim 3.2\ \sigma$) large TF residuals. In this paper, our use of the grouping algorithm accomplished the same thing, albeit in a more objective way. The goal of such exclusion is to restrict the TF and velocity-field analyses to a population of data points whose distribution is, to a reasonable degree, Gaussian. In Paper III we will demonstrate that the TF residuals of our restricted samples have this property. Had we not excluded any objects whatsoever from our analyses, our estimated TF scatters would be marginally higher, and our distribution of residuals unduly weighted by non-Gaussian tails.

The factors influencing TF scatter estimates listed above have been of particular importance when fairly small samples ($N \lesssim 100$) have been considered. The TF samples we have analyzed here have been large: typically several hundred, and, in the case of the MAT sample, over a thousand galaxies. The statistical robustness of our scatter estimates is thus greatly improved. We believe that our final TF scatter estimates are accurate (in an rms sense) to $\lesssim 0.02$ mag for the CCD samples and $\lesssim 0.03$ mag for the H-band A82 sample. This accuracy ensures that the remaining uncertainty will have a very small effect on velocity analyses based on the Mark III catalog.

7.2. *The Intrinsic TF Scatter*

The observed TF scatter reflects photometric and velocity-width measurement errors, as well as intrinsic or "cosmic" scatter. However, it is only the latter quantity that is interesting for studies of spiral galaxy structure and formation (see, e.g., Franx & de Zeeuw 1992; Kauffmann, White, & Guiderdoni 1993; Eisenstein & Loeb 1995). Historically, it has been very difficult to estimate the intrinsic TF scatter because the measurement errors are not fully understood. Using our overlap comparison, however, we have the possibility of separating measurement error from intrinsic scatter and thus estimating the latter.

The dispersions σ_μ listed in column (5) of Table 11 reflect only measurement error since the comparisons were done on a galaxy-by-galaxy basis. Thus, σ_μ represents the TF measurement errors of sample 1 and sample 2 added in quadrature; if these errors are roughly the same for each sample, we can estimate the measurement errors for a given sample. Not all of the overlap comparisons are valid for this purpose. The HM, W91CL, and W91PP samples use mostly the same H I data; consequently, their measurement errors are highly correlated (thus the very small σ_μ values for those comparisons). The CF and W91 samples were designed for maximal photometric consistency and used identical data reduction methods; those two samples, too, may thus be expected to have well-correlated errors. The MAT overlaps with W91PP and W91CL also share H I data. The CCD-based sample comparisons for which the observational errors are fully uncorrelated are CF versus HM and MAT versus HM; these comparisons exhibit dispersions ~0.30–0.34 mag. Thus, the TF measurement error for a CCD sample is given by $\sim 0.32/\sqrt{2} \approx 0.23$ mag.

If we subtract this value in quadrature from the observed TF scatters given in Table 12, we deduce that the intrinsic scatter of the TF relation is ~0.30–0.35 mag. We may go through a similar exercise for the A82 versus others comparison. This leads to an estimate of $\sim(0.44^2 - 0.23^2)^{1/2} \approx 0.37$ mag TF measurement error for the *H*-band sample; subtracting this in quadrature from the observed *H*-band scatter of 0.47 mag gives an intrinsic scatter of ~0.30 mag for the *H*-band TF relation. This estimate is consistent with those obtained from the CCD samples, and it confirms that the *H*-band TF relation has larger observed scatter only because of larger overall measurement errors. We conclude that the intrinsic scatter of the TF relation is $\gtrsim 0.30$ mag. This estimate conflicts strongly with that of Bernstein et al. (1994), who concluded that the TF relation exhibited essentially no intrinsic scatter whatsoever.

8. SUMMARY AND FURTHER DISCUSSION

The main result of this paper is the final calibration of TF relations for the spiral galaxy samples that constitute the backbone of the Mark III Catalog of Galaxy Peculiar Velocities. In Paper I, we obtained a final TF calibration for the HM cluster sample and a provisional (approximate zero point) calibration of the W91CL cluster sample. In this paper we first obtained provisional TF calibrations for the MAT, W91PP, CF, and A82 samples. We then carried out an overlap comparison, using the several hundred galaxies common to two or more samples, to obtain final TF zero points for all samples. The final forward and inverse TF relations are given in Table 12. Indicated are the forward TF parameters *A*, *b*, and σ, and the inverse parameters *D*, *e*, and σ_η (see Paper I, § 2.1). Also indicated, in parentheses, are estimated 1 σ errors in the zero points and slopes; we discuss scatter uncertainty below. In Paper III we will present the TF-distances and peculiar velocities, along with a variety of ancillary data, for all sample objects; these data will be made available for electronic distribution as well.

The estimated zero-point and slope errors warrant further discussion. The error in the HM zero point was based on the assumption that the clusters have random radial motions of 250 km s^{-1} superposed on what is otherwise at most a bulk-flow departure from uniform Hubble expansion. However, as noted in Paper I, a larger error could be present if the mean expansion rate within the effective radius probed by the clusters (~7000 km s^{-1}) differs from the universal expansion rate. Differences at the few percent level are expected simply because of typical mass-density fluctuations. However, since we have no meaningful estimate of the overdensity within our local volume, we have not incorporated such possible errors into the HM zero-point error estimate. Because we have fixed the zero points of the remaining samples ultimately through overlap with HM, *any zero-point error in the HM TF relation will be present in the other TF relations as well.* With this understanding, what is listed in Table 12 for these samples are zero-point errors *relative* to HM, derived from the overlap comparison of § 6. The slope errors listed in Table 12 are simply the statistical errors incurred in the least-squares fits. They are lower limits to the actual slope uncertainties, which also include contributions from the bias-correction procedure and the nonuniqueness of the groups used in calibration. However, the actual slope uncertainties cannot be much larger than those indicated in Table 12 because our analysis of simulated TF samples yielded correct slopes to within the statistical errors computed as above.

As in Paper I, we have carried out careful corrections for sample-selection biases, following the prescription of W94. We have validated these corrections by comparing forward and inverse TF distance moduli for groups of galaxies. We have also used the TF calibration procedure itself to determine the best values of the internal-extinction coefficients, under the assumption that the best value minimizes TF scatter. We have confirmed and strengthened the conclusion of Paper I, namely that $C^I_{\rm int} = C^r_{\rm int} = 0.95$, with relatively small ($\lesssim 0.2$) uncertainty for the *I*-band samples (HM and MAT) and somewhat larger (~0.3) for the *r*-band samples (W91 and CF). Our analysis of the *H*-band TF scatter as a function of extinction coefficient yielded a best value $C^H_{\rm int} = -0.3$; although we adopt this value for A82, the data do not strongly rule out the null value $C^H_{\rm int} = 0$. We have gone beyond the Paper I analysis of internal extinction by testing, using the MAT and W91PP samples, for the luminosity dependence of $C_{\rm int}$ that Giovanelli (1995) has claimed to detect. Our tests did not confirm the

TABLE 12

FINAL TF RELATIONS FOR MARK III SAMPLES

	FORWARD			INVERSE		
SAMPLE	*A*	*b* (±)	σ (mag)	*D* (±)	*e* (±)	σ_η
HM	−5.48 (0.03)	7.87 (0.16)	0.40	−5.58 (0.03)	0.1177 (0.0025)	0.048
W19CL......	−4.18 (0.02)	7.73 (0.21)	0.38	−4.27 (0.02)	0.1190 (0.0032)	0.047
W91PP......	−4.28 (0.02)	7.12 (0.18)	0.38	−4.36 (0.02)	0.1244 (0.0031)	0.049
CF	−4.22 (0.02)	7.73 (0.21)	0.38	−4.33 (0.02)	0.1190 (0.0032)	0.047
MAT	−5.79 (0.03)	6.80 (0.08)	0.43	−5.92 (0.03)	0.1328 (0.0016)	0.059
A82	−5.95 (0.04)	10.29 (0.22)	0.47	−6.03 (0.04)	0.0893 (0.0018)	0.043

NOTE.—Parameters of the fully calibrated TF relations for the Mark III spiral samples.

existence of this effect; instead, they show that internal extinction depends on axial ratio alone.

We have emphasized the importance of accurately estimating TF scatter and have accordingly treated it as part and parcel of the TF calibration. We suggested that divergent estimates of $\sigma_{\rm TF}$ in the past stemmed from widely differing strategies for modeling relative galaxy distances and excluding unwanted outliers. We have attempted to rationalize these issues by means of a self-consistent procedure that combines the grouping of field galaxies with TF calibration. To the degree that we succeeded in constructing groups of objects with a common distance, our TF scatter estimates should be valid; application of our methods to simulated catalogs suggests that these estimates are in fact good to $\lesssim 0.02$–0.03 mag. In this paper we found $\sigma_{\rm TF} \approx 0.38$–$0.43$ mag for the CCD data sets, consistent with our Paper I results for the cluster samples. This is significantly higher than many of the more optimistic estimates of recent years, and we believe it to be more realistic. Using the results of our overlap analysis, we estimated the intrinsic or "cosmic" TF scatter to be ~ 0.30 mag. If correct, this value places strong constraints on theories of spiral galaxy formation.

We would like to thank Michael Strauss for helpful comments on the paper. This work has been partially supported by the US-Israel Binational Science Foundation and NSF grant PHY-91-06678. D. B. wishes to acknowledge partial support from NSF grant AST-9016930.

REFERENCES

Aaronson, M., Bothun, G. D., Mould, J. R., Huchra, J. P., Schommer, R. A., & Cornell, M. E. 1986, ApJ, 302, 536

Aaronson, M., Huchra, J. P., Mould, J. R., Schechter, P. L., & Tully, R. B. 1982, ApJ, 258, 64

Aaronson, M., Mould, J. R., Huchra, J. P., Sullivan, W. T., III, Schommer, R. A., & Bothun, G. D. 1980, ApJ, 239, 12

Babul, A., Weinberg, D. H., Dekel, A., & Ostriker, J. P. 1994, ApJ, 427, 1

Bernstein, G. M., Guhathakurta, P., Raychaudhury, S., Giovanelli, R., Haynes, M. P., Herter, T., & Vogt, N. P. 1994, AJ, 107, 1962

Bothun, G. D., & Mould, J. R. 1987, ApJ, 313, 629

Courteau, S. 1992, Ph.D. thesis, Univ. California, Santa Cruz

———. 1996, ApJS, in press

Courteau, S., Faber, S. M., Dressler, A., & Willick, J. A. 1993, ApJ, 412, L51

Dekel, A. 1994, ARA&A, 32, 371

Dekel, A., Bertschinger, E., & Faber, S. M. 1990, ApJ, 364, 349

Dekel, A., Bertschinger, E., Yahil, A., Strauss, M. A., Davis, M., & Huchra, J. P. 1993, ApJ, 412, 1

Dekel, A., et al. 1996, in preparation (Paper V)

Eisenstein, D. J., & Loeb, A. 1995, in preparation

Faber, S. M., Courteau, S., Dekel, A., Dressler, A., Kolatt, T., Willick, J. A., & Yahil, A. 1993, in Cosmic Velocity Fields, ed. F. R. Bouchet & M. Lachiéze-Rey (Gif-sur-Yvette: Ed. Frontiéres), 15

———. 1994, JRASC, 88, 92

Faber, S. M., et al. 1996, in preparation (Paper IV).

Federspiel, M., Sandage, A., & Tammann, G. A. 1994, ApJ, 430, 29

Franx, M., & de Zeeuw, T. 1992, ApJ, 392, L47

Giovanelli, R. 1995, in The Opacity of Spiral Disks, ed. J. I. Davies & D. Burstein (NATO ASI Ser. C, 469) (Dordrecht: Kluwer), 127

Giovanelli, R., & Haynes, M. P. 1985, AJ, 90, 2445 (GH)

———. 1989, AJ, 97, 633 (GH)

Giovanelli, R., Haynes, M. P., Charmaraux, P., da Costa, L. N., Freuding, W., Salzer, J. J., & Wegner, G. 1995, IAU Symp. 168, preprint

Giovanelli, R., Haynes, M. P., Myers, S. T., & Roth, J. 1986a, AJ, 92, 250 (GH)

Giovanelli, R., Haynes, M. P., Rubin, V. C., & Ford, W. K., Jr. 1986b, ApJ, 301, L7 (GH)

Górski, K. M., Hinshaw, G., Banday, A. J., Bennett, C. L., Wright, E. L., Kogut, A., Smoot, G. F., & Lubin, P. 1994, ApJ, 430, L89

Hudson, M. J., Dekel, A., Courteau, S., Faber, S. M., & Willick, J. A. 1995, MNRAS, 274, 305

Kauffmann, G., White, S. D. M., & Guiderdoni, B. 1993, MNRAS, 264, 201

Kolatt, T. 1995, Ph.D. thesis, Hebrew Univ. Jersalem

Kolatt, T., Dekel, A., Ganon, G., & Willick, J. A. 1996, ApJ, in press

Lahav, O., Rowan-Robinson, M., & Lynden-Bell, D. 1988, MNRAS, 234, 677

Lauberts, A. 1982, The ESO/Uppsala Survey of the ESO (B) Atlas (Munich: ESO)

Mathewson, D. S., Ford, V. L., & Buchhorn, M. 1992, ApJS, 81, 413 (MAT92)

Nilson, P. 1973, Uppsala General Catalogue of Galaxies (Uppsala: Uppsala Obs. Ann.)

Pierce, M. J., & Tully, R. B. 1988, ApJ, 330, 579

Sandage, A. 1994, ApJ, 430, 13

Schommer, R. A., Bothun, G. D., Williams, T. B., & Mould, J. R. 1993, AJ, 105, 97

Strauss, M. A., & Willick, J. A. 1995, Phys. Rep., in press

Tormen, B., & Burstein, D. 1995, ApJS, 96, 123 (TB95)

Vorontsov-Veliaminov, B. A., & Arhipova, V. P. 1968, Morphological Catalogue of Galaxies (Moscow: Moscow Univ. Press)

Willick, J. A. 1991, Ph.D. thesis, Univ. California, Berkeley

———. 1994, ApJS, 92, 1 (W94)

Willick, J. A., Courteau, S., Faber, S. M., Burstein, D., & Dekel, A. 1995a, ApJ, 446, 12 (Paper I)

Willick, J. A., et al. 1995b, in preparation (Paper III)

Zwicky, F., Herzog, E., Karpowicz, M., Kowal, C. T., & Wild, P. 1961–1968, Catalogue of Galaxies and Clusters of Galaxies (Pasadena: Caltech)